ACS OMEGA

Open Access

http://pubs.acs.org/journal/acsodf

Article

Multiobjective Optimization Strategy for Enhancing the Efficiency and Quality of Organic Thin-Film Manufacturing with Electrohydrodynamic Atomization Coating

Chao Hu, Jiankui Chen,* Wei Chen, Wei Tang, Guozhen Wang, Fei Pan, and Zhouping Yin

Cite This: *ACS Omega* 2024, 9, 38970−38988

Read Online

ACCESS | Metrics & More | Article Recommendations

ABSTRACT: Electrohydrodynamic atomization coating technology is well-suited for micro-/nanoscale thin-film additive manufacturing. However, there are still some challenges in quality control and parameter adjustment during the coating process. Especially when coating on nonconductive and nonhydrophilic substrates, film quality and thickness uniformity are difficult to control. This paper proposes an optimization strategy for enhancing the efficiency and quality of thin-film manufacturing on nonconductive, nonhydrophilic glass substrates. In this paper, a visual inspection system was developed for in situ inspection and identification of droplet deposition states in the substrate surface. Then, the statistical relationship between the operating parameters and the quality of the deposition state was analyzed by response surface methodology. On this basis, machine learning models and intelligent recommendation frameworks for small data sets were developed to rapidly optimize operating parameters and improve the quality of thin-film coating. Optimization strategy developed by applying the principles of statistical modeling, analysis of variance, and global optimization are more efficient and less costly than traditional parameter screening methods. The experimental results show that optimum deposition quality can be obtained with the recommended operating parameters. And, validation results show a 12.8% improvement in film thickness uniformity. At the same time, no mura defects appeared on the thin-film surface. The proposed optimization strategy can improve the efficiency and quality of additive manufacturing of micro and nano thin films and is beneficial for advancing industrial applications of the electrohydrodynamic atomization coating.

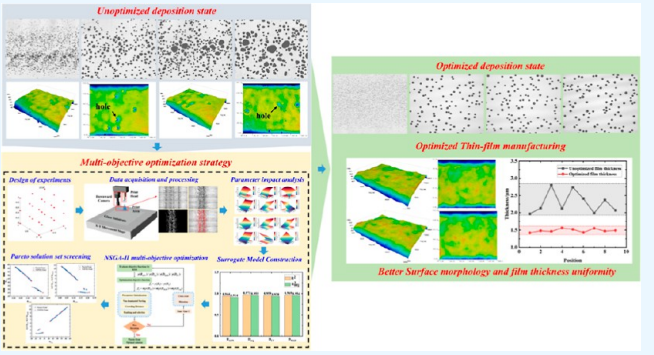

1. INTRODUCTION

Electrohydrodynamic atomization coating (EHDAC) as a continuous noncontact coating technique is well-suited for thin-film additive manufacturing on 3D or anisotropic surfaces. The EHDAC process offers significant advantages in terms of fabrication principles over conventional manufacturing processes when oriented toward the fabrication of micro- and nanoscale thin films.[1,2] On the one hand, the micro- and nanoscale droplets formed by the EHDAC have the same charge and can be charged up to a fraction of the Rayleigh limit $Q_r = 2\pi(16\sigma_l\varepsilon_0 r_d^3)^{1/2}$, where σ_l is the surface tension of liquid, ε_0 is the electrical permittivity of the free space, and r_d is the droplet radius.[3] Due to the interaction of Coulomb forces, the droplets are highly dispersed in space and can form a certain atomization range.[4] The motion of a charged droplet in the axial direction can be described with $m_d\frac{dv_d}{dt} = F_G + F_D + F_E + F_C$, where m_d is the mass of droplets, v_d is the velocity of droplets, F_G and F_D are the gravity force and the drag force on droplets, respectively, and F_E and F_C are the electric field force due to applying an external electric field and the interaction force between droplets due to Coulomb repulsion, respectively.[5] On the other hand, controlling the movement of the charged droplet clusters through an electric field can reduce material loss and improve manufacturing efficiency.[6] This sustainable green coating technology is now widely used in additive manufacturing,[7,8] flexible electronics,[9−11] biomedical,[12,13] and new energy sources.[14,15]

By adjustment of the parameters, the EHDAC technology can create different spray modes and deposition patterns. When the target ink is identified, the liquid supply and the magnitude of the electrical stress at the gas−liquid interface can be adjusted to achieve a shift in the spraying modes of

Received: June 10, 2024
Revised: August 22, 2024
Accepted: August 29, 2024
Published: September 6, 2024

dripping, micro dripping, cone-jet, etc.[16,17] Different operating modes produce droplets with different size distributions. Parameter adjustments can also produce well-controlled monodisperse droplets and narrower size distributions of droplet clusters.[18,19] The deposition of droplets of different sizes results in different patterns on the target substrate. Although the EHDAC has many advantages and is used in a wide range of applications. However, as a complex, multistage hydrodynamic process, there are still some issues that limit its development in applications. For example, when coating on nonconductive and nonhydrophilic substrates, the charge accumulation and repulsion due to the electrically charged droplets result in poor quality films. And, the advantages of the EHDAC process in terms of its wide range of multiparameter adjustability may cause some trouble at the design stage, which is a double-edged sword restricting the development of the EHDAC. Complex fluid dynamics problems across scales with high demands on measurement techniques pose a great challenge for controlling the quality of the coating process. At the same time, operating parameters have a significant impact on the process, and quickly adjusting the coating parameters is a key issue to consider.

To improve the manufacturing quality of the EHDAC process, many methods have been explored to investigate parameter control methods. Hayati et al.[20] reported an experimental study of the interactions between the EHDAC model and several parameters and analyzed the formation of stable jets and the stability of coating. Huo et al.[21] used a high-speed camera to visualize the spray state of coating. It was found that the spray pattern shift depends on the number of electric bonds, which is mainly determined by the coating voltage and coating height. Yang et al.[22] used expensive visualization to investigate the instability of jet fragmentation in EHDAC. Wang et al.[23] reported that a stable spray pattern was obtained by analyzing the effect of operating parameters through a lot of trial-and-error experiments. Virtually, all the advantages of the EHDAC process depend on the distribution of the charged droplet clusters after atomization.[24] The droplet size distribution and scaling law during the EHDAC process were also investigated. Tang and Gomez.[25] reported the inspection of the size distribution and flight velocity of charged droplet clusters during coating through a phase Doppler anemometry device. A theoretical method to control the electrospray structure was also explored. Leeuwenburgh et al.[26] reported that the size distribution of the charged droplet clusters during EHDAC was monitored by a phase Doppler anemometry device to adjust the parameters to form different film morphologies. The coating parameters are adjusted by directly detecting the jetting state and the fission process. However, the studies presented above lacked quality control and parameter regulation methods.

Conditioning methods for the direct measurement of film quality are more dependent on high-precision measuring equipment. Characterization and judgment of the target state at the micro- and nanoscale is required to find the appropriate combination of interrelated parameters. Kingsley and Chiarot.[27] reported the study of polyimide film deposition states on silicon substrates under different parameters by SEM imaging. Wang et al.[28] investigated the effects of atomization distance, operating voltage, and the flow rate on the properties of deposited films. Under the optimized deposition parameters, uniform and dense films with about a 10-layer structure were prepared. Rietveld et al.[29,30] systematically analyzed the effect of process parameters on the morphology and roughness of the deposited surface by imaging observations. They also analyzed the deposition state under different process parameters to obtain the optimal parameters for polymer film fabrication. Sındıraç and Akkurt.[31] used SEM and secondary electron imaging for microstructural and compositional analyses of sample cross sections to obtain optimal EHDAC process parameters and deposition quality. In the above study, the inspection process would consume a lot of time and resources and the need to transfer substrates would not allow for in situ inspection. The method of adjusting the operating parameters is based on trial-and-error experiments, and there is a lack of discriminative methods with generality.[32] Without modeling, there will be a strong reliance on prior operational experience.

Currently, statistical-data-driven quality control and optimization methods are widely used. For example, Zhang et al.[33] achieved a multiobjective optimization of the quality of the aerosol coating process using response surface methodology (RSM). Singh et al.[34] analyzed and optimized process parameters for 3D coating using RSM. And, machine learning methods can quickly assist in modeling and learning predictions. Suzuki et al.[35] used machine learning methods to optimize the process parameters for controlling the microstructure in a laser powder bed fused WC/Co cemented carbide. Liu et al.[36] achieved quality optimization of the aerosol 3D coating process by building a machine learning framework. To the best of our knowledge, there are currently few applications of these methods in the EHDAC.

This work proposes an optimization framework based on data statistics and machine learning to explore the potential application of data-driven quality control methods in the EHDAC process. In the optimization strategy, experimental design and response analysis methods have been used to investigate the effect of manipulation on the deposition state, which can reduce experimental costs. Consumption of significant resources is due to high demand for the inspection process. In this paper, a new inspection method and system for the in situ inspection of the deposition state was developed based on the principles of the EHDAC. Four parameters are proposed to quickly describe the deposition quality of the charged droplet clusters in the EHDAC process. The RSM models were constructed to analyze the intrinsic relationship between operational parameters and the quality of the depositional state. Furthermore, there was development of a machine learning model and intelligent recommendation framework based on small data sets for the rapid optimization of operating parameters to improve the quality of thin-film manufacturing. Till now, there have been few systematic studies on coating quality optimization of the EHDAC process. This research attempts to contribute to enriching the body of knowledge on EHDAC quality optimization. To promote the application of intelligent methods in the coating process and provide new quality control solutions for coating on nonconductive, nonhydrophilic glass substrates.

The paper is organized as follows: Section 2 describes the research problem and the proposed multiobjective optimization framework. The experimental system, model performance, and multiobjective optimization framework results are discussed in detail in Section 3. At the same time, the process of parameter optimization recommendation and experimental comparison results are presented. Conclusions are presented in Section 4.

https://doi.org/10.1021/acsomega.4c05402
ACS Omega 2024, 9, 38970−38988

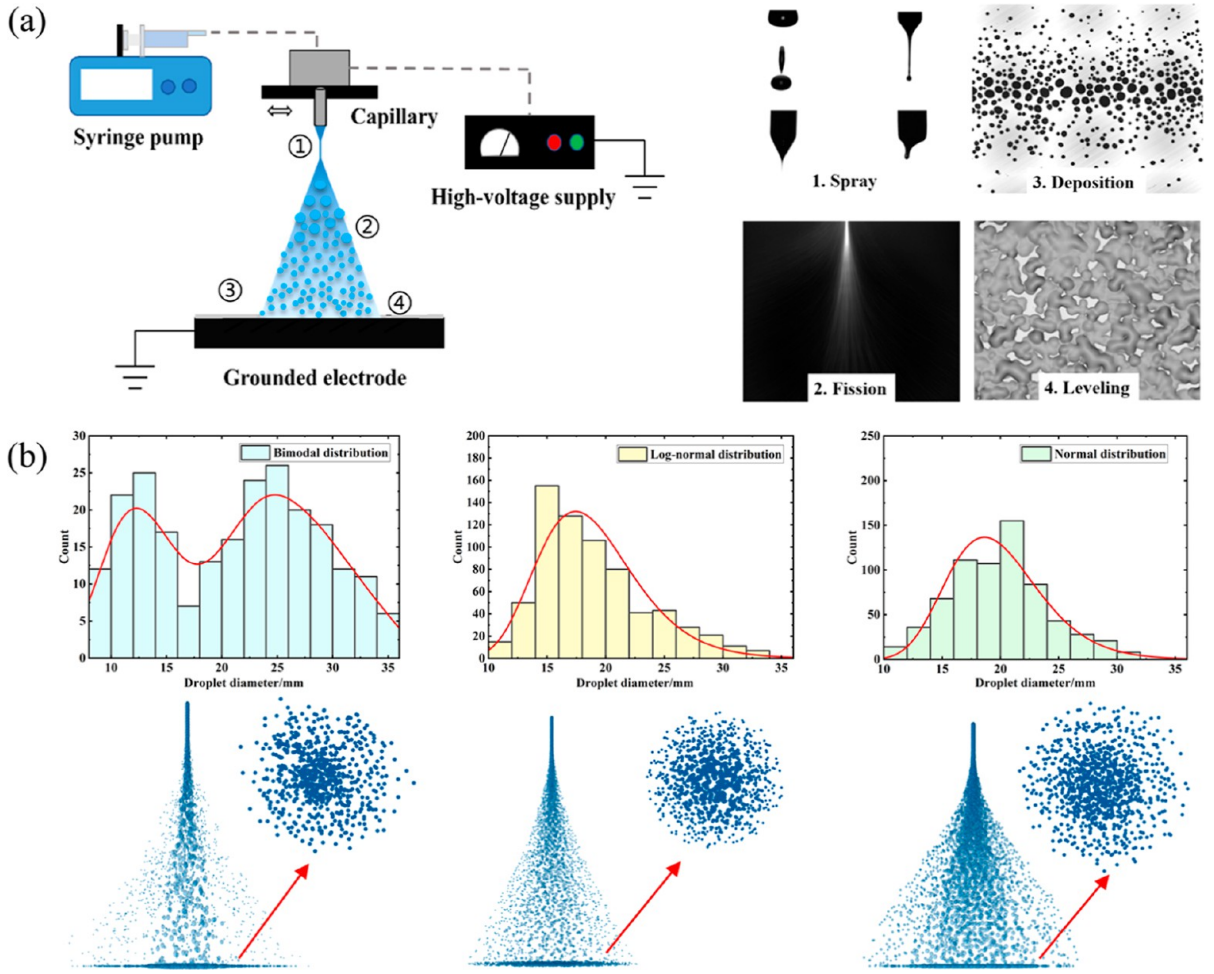

Figure 1. (a) Schematic diagram of the EHDAC process. (b) Deposition of charged droplet clusters with different size distributions.

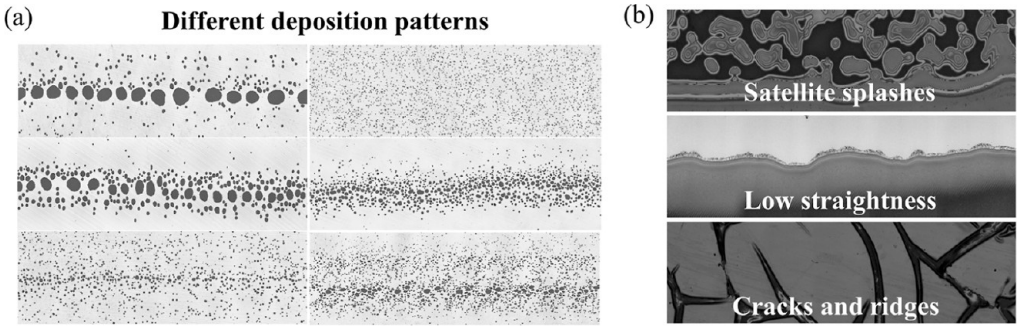

Figure 2. (a) Deposition patterns and (b) film defects.

2. METHODOLOGY

2.1. Problem Formulation. The EHDAC is an advanced deposition technology for continuous additive coating of thin-film structures. The setup principle of the EHDAC is shown in Figure 1a, under the action of the coupling field, the charged droplets will go through spraying, fission, deposition, and leveling. Differences in fluid rheology exist at different operating parameters. The first thing that changes is the spray pattern at the tip of the capillary. Then, due to the size separation effect in the droplet fission process,[37] as shown in Figure 1b, the EHDAC creates charged droplet clusters with different size distributions in space. And, when charged droplet clusters are deposited, various coating patterns appear. This phenomenon is more pronounced on nonconductive and nonhydrophilic substrates, as shown in Figure 2a. The degree of dispersion, distribution of spreading, and homogeneity of the charged droplet clusters are different for different deposition patterns.[38] Uniform dispersion of the droplets resulted in a film of uniform thickness. On the contrary, as shown in Figure 2b, inhomogeneous droplet deposition, after leveling and curing, can cause serious problems such as mura defects and even cracks in the film.

To obtain high-quality deposition, it is necessary to investigate the deposition characteristics of charged droplet clusters on a nonconductive and nonhydrophilic glass substrate. In this paper, a schematic diagram describing the

https://doi.org/10.1021/acsomega.4c05402
ACS Omega 2024, 9, 38970−38988

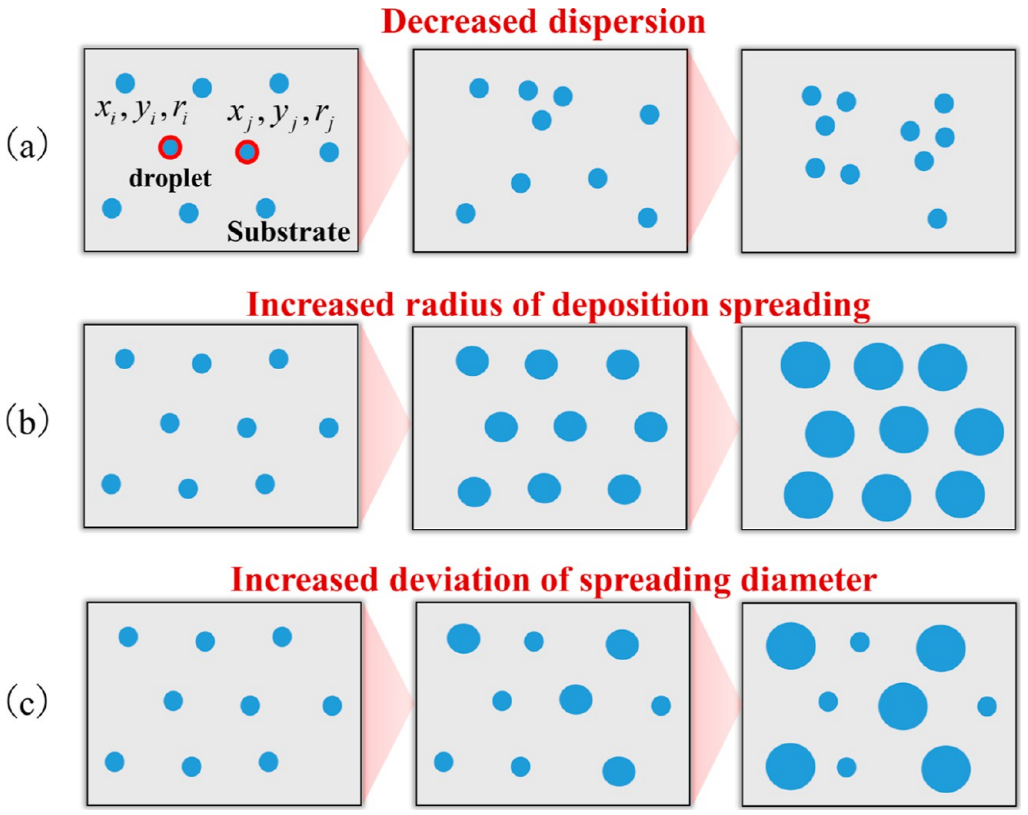

Figure 3. Changes in the deposition state of the charged droplets: (a) different dispersion, (b) different spreading radius, and (c) different spreading radius deviations.

deposition spreading state of the charged droplet clusters is shown in Figure 3. The dispersion and spreading diameter distributions of droplet clusters change with operating parameters. Due to the difference in volume and spatial distribution of the charged drops, the force and direction of motion of the droplets under the coupling effect of the field are different. Smaller volumes of charged droplets have higher radial flight velocity under the repulsion of Coulomb force and will be dispersed at the edge of the atomization region. The larger charged droplets have a higher axial flight velocity due to gravity and are more aggregated after deposition. The properties exhibited by the droplets in different deposition patterns are different. This difference is described by defining four parameters. The average nearest neighbor R_{ANN} is used to describe the dispersion of charged droplet clusters. The average spreading diameter D_{avg}, the coefficient of variation of spreading diameter D_{CV}, and the mean absolute deviation of spreading diameter D_{MAD} were used to evaluate the uniformity of the deposition of charged droplet clusters. For the deposited droplet clusters, assume that the droplets are deposited at a coordinate value of x_i and y_i, the spreading radius is r_i, and the average nearest neighbor based on the Euclidean distance is calculated as follows

$$R_{ANN} = \frac{\overline{d_0}}{\overline{d_E}} \tag{1}$$

$$d_i = \sqrt{(x_i - x_j)^2 + (y_i - y_j)^2} \tag{2}$$

$$\overline{d_0} = \frac{\sum_{i=1}^{n} d_i}{z} \tag{3}$$

$$\overline{d_E} = \frac{0.5}{\sqrt{z/S}} \tag{4}$$

where $\overline{d_0}$ represents the average distance between the droplet and the other, $\overline{d_E}$ represents the expected average distance between droplets in a random distribution pattern, z represents the number of droplets, and S represents the area of the droplet cluster deposition pattern. The smaller the value of the R_{ANN}, the lower the degree of dispersion between droplets and conversely the higher the dispersion. In the coating process, the deposition of charged droplet clusters should have a lower degree of dispersion. Otherwise, defects such as scattering, mura, etc. will occur.

Evaluation parameters D_{avg}, D_{CV}, and D_{MAD} will be calculated using eqs 5, 6, and 7. D_{avg} represents the scale of droplet fission during the EHDAC process. D_{CV} and D_{MAD} were used to describe the uniformity of the distribution of the spreading droplets. The higher the quality of the EHDAC process, the smaller the spreading diameter and the deviation of the spreading diameter of the charged droplets.

$$D_{avg} = \frac{2}{z}\sum_{i=1}^{z} r_i \tag{5}$$

$$D_{CV} = \frac{\sqrt{\sum_{i=1}^{z}(2r_i - D_{avg})^2/(z-1)}}{D_{avg}} \tag{6}$$

$$D_{MAD} = \frac{1}{z}\sum_{i=1}^{z}|2r_i - D_{avg}| \tag{7}$$

https://doi.org/10.1021/acsomega.4c05402
ACS Omega 2024, 9, 38970−38988

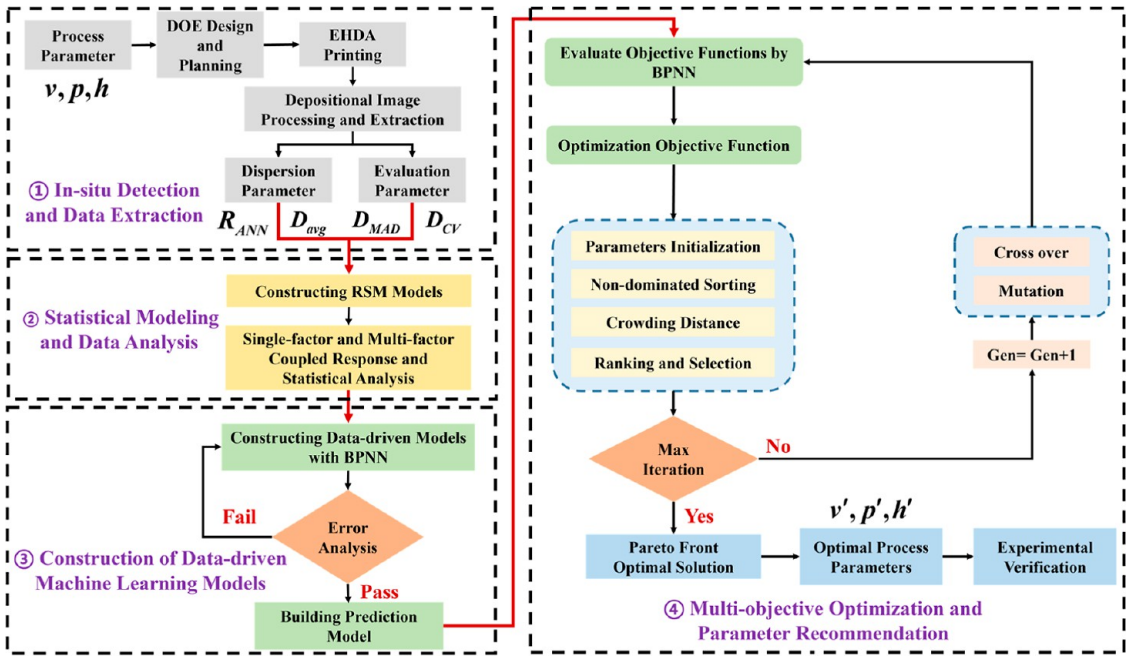

Figure 4. Schematic diagram of the multiobjective optimization strategy framework.

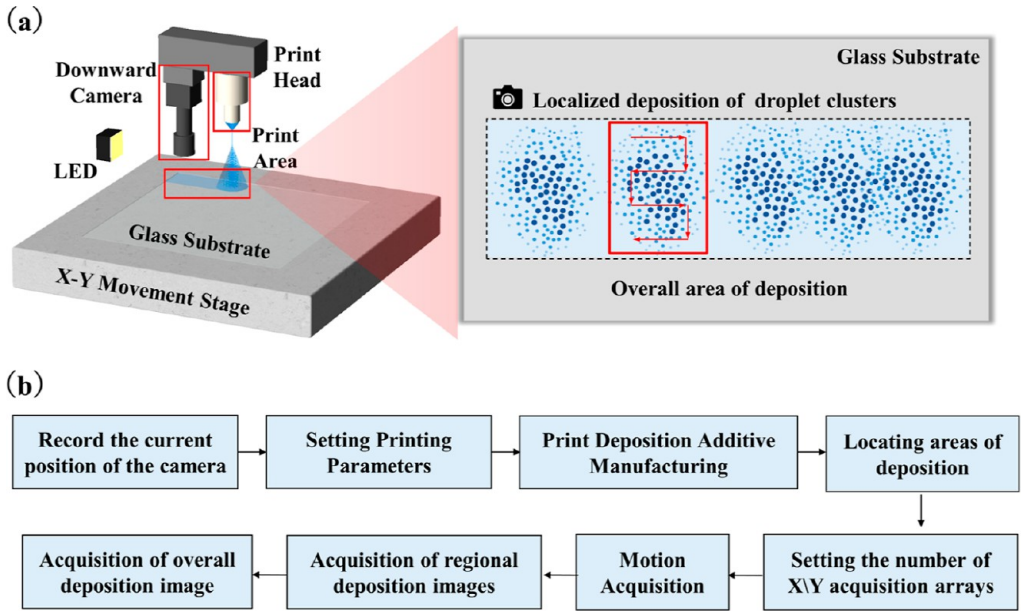

Figure 5. (a) Schematic diagram of the acquisition system and (b) logic of acquisition.

The diverse deposition states of the charged droplet clusters contain a large amount of data information. New modeling and optimization methods based on data science drive have great potential for efficient process optimization. Conventional methods are difficult to observe, and these complex the fluid rheological process. A system optimization framework integrating advanced technologies must be developed to fully optimize the EHDAC process.

2.2. Multiobjective Optimization Framework. As shown in Figure 4, the proposed multiobjective optimization framework consists of four stages: (1) In situ inspection and data extraction. Inspection during the coating process is a better way to control the quality of the manufacturing process. By acquiring images of droplet deposition and extracting them using digital image processing methods, the required data information can be quickly obtained. (2) Statistical modeling and data analysis. The extracted data information is modeled and analyzed to investigate the influence of single factors and coupling effects on the deposition quality during the coating process. Statistical analysis methods are robust when geared toward data mining. (3) Construction of data-driven machine learning models. Data-driven network models based on small data sets have higher accuracy and provide a basis for subsequent multiobjective optimization. (4) Multiobjective optimization and parameter recommendation. Application of nondominated sorting algorithms to deposition quality optimization to satisfy multiple objectives to be optimized. After the optimal set of solutions in the parameter space is

https://doi.org/10.1021/acsomega.4c05402
ACS Omega 2024, 9, 38970−38988

obtained, the optimal operating parameters and the optimal deposition quality are finally obtained by intelligent screening methods.

2.3. In Situ Deposition Data Acquisition System. By detecting the deposition state of droplet clusters, it can be used as a new way to judge coating quality. For example, Zhang et al.[39] proposed a method to detect the deposition state of charged droplet clusters for quality control. To improve the efficiency of process inspection and data collection, this paper proposes the use of in situ inspection methods to collect the droplet deposition state. In situ measurement avoids transferring the substrate and interfering with subsequent coating. The acquisition of the deposition state of the charged droplet clusters is achieved by constructing an in situ inspection system. The schematic diagram of the acquisition system is shown in Figure 5a. The system consists of a CCD camera, LED light source, coating device, and motion platform. Logic for acquiring deposited images is calibrated, printed, positioned, and acquired in arrays, as shown in Figure 5b. By positioning the coating area and setting the X and Y direction scanning steps of the downward-facing camera, the deposited image of the coating under different operating parameters is captured. And, digital image processing algorithms are used to further process the data present in the deposited image. The digital image processing flow is shown in Figure 6. First, the

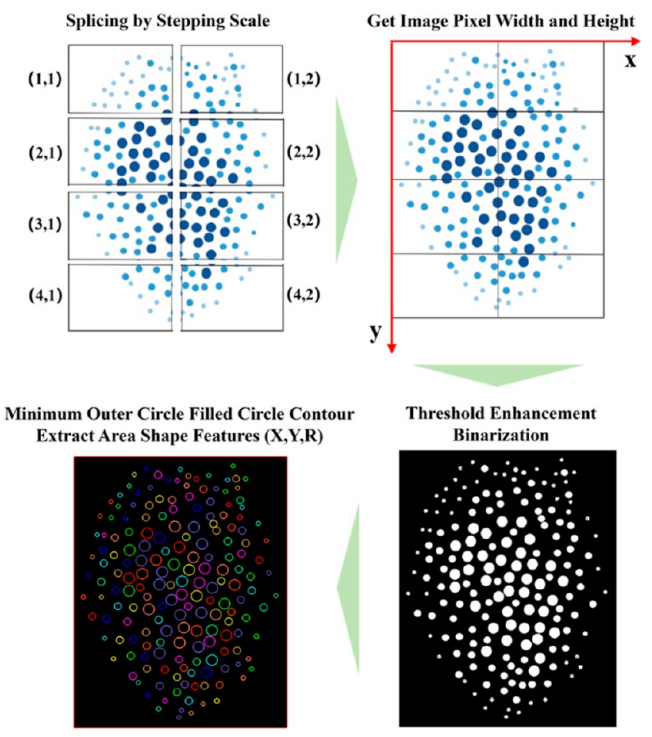

Figure 6. Processing and parameter extraction of the depositional images.

local deposition images were stitched to obtain the overall deposition image. Subsequently, the overall deposited image was subjected to threshold-enhanced binarization and morphological filling. Finally, the coordinates and diameters of the deposited distribution droplets are extracted, and the corresponding parameters can be calculated. The processing operations such as image stitching, extraction of dimensions, threshold enhancement and binarization, minimum outer circle fitting, and circle parameter extraction are processed using Halcon-21.11 software. The number of pixels n_{pixel} extracted from the deposited image is converted to its actual size L by the formula

$$L = \frac{n_{\text{pixel}} l_{\text{pixel}}}{m_{\text{h}}} \tag{8}$$

where l_{pixel} represents the pixel size of the camera and m_{h} represents the magnification of the camera lens. Since the droplet spread is not necessarily a regular circle, there will be some recognition errors in the image processing. However, the number of droplets is large, and this part of the error will be negligible when statistical calculations are performed.

2.4. Response Surface Methodology Based on Statistical Data. The state and quality of EHDAC are the result of the coupling between parameters. By constructing relationships between inputs and responses, it is possible to study the influence of single factors and coupled effects. Linking inputs and outputs with functions can be used to perform complex iterative calculations. This approach can be used instead of solving real-world problems. Models are generally implemented based on fitting and interpolation by constructing a hypersurface approach from actual values at multiple sampling points. In order to determine the effects and sensitivities of the operating parameters and analyze whether there are any interactions between the parameters, the RSM method will be used.[40] Response surface models are constructed by using experimental design and statistical ideas. High fidelity of the model can be ensured by the design of experiments to generate suitable sample points.[41] Since EHDAC is a complex nonlinear process, a full factorial orthogonal array with 27 sample points will be used for the trial planning design.[42] This method reduces the nonlinearity of the problem.[43] The general form of the RSM model is shown in eq 9, where β_0, β_i, and β_{ii} are the coefficients; ε is the statistical error; and M represents the number of factors. The RSM model was tested for significance by ANOVA methods.

$$Y = \beta_0 + \sum_{i=1}^{M} \beta_i X_i + \sum_{i} \sum_{j} \beta_{ij} X_i X_j + \sum_{i=1}^{M} \beta_{ii} X_i^2 + \varepsilon,\ i < j \tag{9}$$

2.5. Data-Driven Machine Learning Agent Models. Data-driven models use samples of collected variables to infer relationships between variables in reverse. By using preprocessing methods such as normalization and downsampling for samples of known variables, the physical nature of the real problem can be disregarded.[44,45] To further construct a data-driven model between operation parameters and deposition quality, the model construction will be carried out by BPNN. The proposed four descriptive parameters will be used as the output layer and the operational parameters as the input layer.

BPNN is an artificial neural network model, invented due to the inspiration of the workings of biological neurons. It is very widely used and can be used without knowing the correspondence between the input data and output data. BPNN learns a certain mapping relationship between the input data and the output data only through continuous iterative training and can calculate the result closest to the corresponding output value when given certain input data. And, it shows some generality, i.e., when given similar data but beyond the input range, it can also calculate more accurate output results. Moreover, good performance is guaranteed for small data sets as well. Such a powerful feature is attributed to

https://doi.org/10.1021/acsomega.4c05402
ACS Omega 2024, 9, 38970−38988

the forward transfer result and backward transfer error of BPNN. The BPNN computes the final prediction during forward propagation, calculates the loss function values based on a given certain loss function, and calculates the partial derivatives of each parameter. At the same time, the bias of the loss function, with respect to the weights and thresholds, is calculated by the chain rule. The learning rate is later combined to update the weights and thresholds of the neurons in each layer. This process will be iterated until the value of the loss function reaches a certain range, and the network model tends to converge.

As a result, rapid modeling of deposition quality using BPNN has the unique advantage of reducing a large amount of physical equation modeling effort.[46] A typical BPNN network structure is shown in Figure 7. The data collected during the

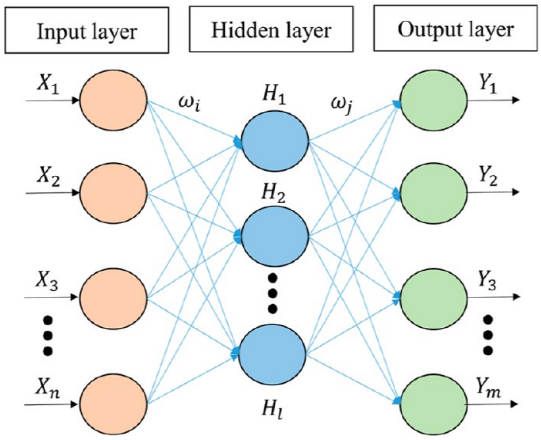

Figure 7. Schematic diagram of the BPNN model.

coating process need to be preprocessed by normalization to avoid affecting the results of model training. The normalized preprocessing is calculated by eqs 10 and 11, where D_{max} is the maximum value of the input parameter, D_{min} is the minimum value of the input parameter, $\overline{D}$ is the average value of the input parameter, and D_i is the ith set of input parameters. The loss function of BPNN is calculated using the mean square error. In order to improve the optimization efficiency of BPNN, this paper used Nesterov's method for iterative computation.[47] The Nesterov's method is a commonly used gradient descent optimization method that is based on a small variant of the momentum optimization algorithm. Compared to other optimization methods, Nesterov's method provides faster training and accelerates the convergence of the model. The accuracy of the data-driven model is evaluated using R^2 and R^2_{adj}. The formulas are shown in eqs 12−15, where s represents the number of samples.

2.6. Multiobjective Optimization and Intelligent Recommendation.

$$\overline{D} = \frac{D_{max} + D_{min}}{2} \tag{10}$$

$$\tilde{D} = \frac{\tilde{D} - \overline{D}}{d_{max} - \overline{D}} \tag{11}$$

$$R^2 = 1 - \frac{SS_E}{SS_T} \tag{12}$$

$$SS_E = \sum_{q=1}^{s} (Y_q - \widehat{Y_q})^2 \tag{13}$$

$$SS_T = \sum_{q=1}^{s} Y_q^2 - \frac{(\sum_{q=1}^{s} Y_q)^2}{s} \tag{14}$$

$$R^2_{adj} = 1 - \frac{SS_E/(s-M)}{SS_T/(s-1)} = 1 - \frac{s-1}{s-M}(1-R^2) \tag{15}$$

Coating high-quality, high-uniformity, and dense thin films requires that charged droplet clusters be deposited with a small spread radius and a narrow size distribution. At the same time, the deposition range of the droplet clusters should be concentrated. Therefore, a multiobjective optimization function as shown in eq 16 is defined. Analytical models are constructed in the space of the operating parameters of thin-film manufacturing. And, constraint value ranges are added to the objective function.

However, the optimization objectives in the form of eq 16 are more difficult and not easy to solve. Competition between optimization objectives often comes at the expense of another optimization objective and is prone to imprecise optimization solutions. The weighting method is introduced here for modification.[48] By introduction of two weight coefficients, the two deposition evaluation functions D_{CV} and D_{MAD} are converted into one optimization objective. The optimization objective after reducing the solution dimension is shown in eq 17.

$$\min\begin{cases} \mathrm{Obj}_1(R_{ANN}) \\ \mathrm{Obj}_2(D_{avg}) \\ \mathrm{Obj}_3(D_{CV}) \\ \mathrm{Obj}_4(D_{MAD}) \end{cases} ; \text{ s. t. } \begin{cases} v_{min} < v < v_{max},\ v \in 10 \times N \\ p_{min} < p < p_{max},\ p \in 0.1 \times N \\ h_{min} < h < h_{max},\ h \in 0.1 \times N \end{cases} \tag{16}$$

$$\min\begin{cases} \mathrm{Obj}_1(R_{ANN}) \\ \mathrm{Obj}_2(D_{avg}) \\ \mathrm{Obj}_3(\omega_1(D_{CV}) + \omega_2(D_{MAD})) \end{cases} ; \text{ s. t. } \begin{cases} v_{min} < v < v_{max},\ v \in 10 \times N \\ p_{min} < p < p_{max},\ p \in 0.1 \times N \\ h_{min} < h < h_{max},\ h \in 0.1 \times N \\ \omega_1 + \omega_2 = 1 \end{cases} \tag{17}$$

After transformation of a complex real-world problem into an optimization problem, a compromise solution set can be obtained by solving the objective optimization function. The optimization strategy uses the NSGA-II algorithm to search for the optimal set in the constraint parameter space. The NSGA-II is one of the most popular genetic algorithms for solving multiobjective optimization problems in recent years. It is a less costly and efficient method to obtain the Pareto front solution set by nondominated ordering and congestion calculation.[49,50]

The ultimate goal of multiobjective optimization is to obtain a Pareto front solution set. Using an additional decision-

https://doi.org/10.1021/acsomega.4c05402
ACS Omega 2024, 9, 38970−38988

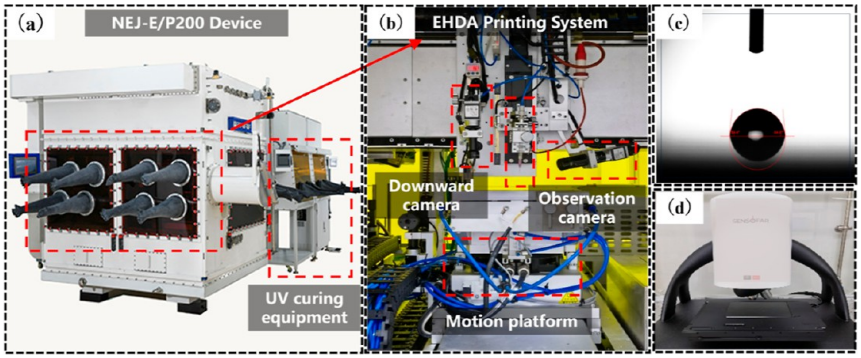

Figure 8. Schematic diagram of EHDAC equipment and experimental conditions: (a) NEJ-E/P200 equipment, (b) EHDAC system, (c) contact angle inspection, and (d) 3D optical profiler.

making method to evaluate the leveling of the solution set, a solution from the set of Pareto front solutions can be recommended as the final optimal solution.[51] This solution is mapped to give the optimal operating parameters. The entropy weight TOPSIS method is used as a standard decision-making method in the optimization strategy.[52] The method uses information entropy to assign weights to the objectives of the optimization model. Using the rule of comparing positive and negative ideal scenarios, the leveling is done by comparing the proximity of the ideal targets. If one of the results is closest to the positive ideal solution (PIS), then it is far away from the negative ideal solution (NIS). This result is the optimal compromise among the results. The decision steps of the entropy weight TOPSIS method are as follows.

Step 1. Defining an evaluation matrix D consisting of m solutions and n objectives and normalizing the matrix:

$$D = (d_{ij})_{m\times n}\{i = 1, 2, \cdots, m; j = 1, 2, \cdots, n\} \tag{18}$$

$$R_{ij} = \frac{d_{ij}}{\sqrt{\sum_{i=1}^{m} d_{ij}^2}} \tag{19}$$

Step 2. Constructing the weighted normalized decision matrix:

$$v_{ij} = w_j R_{ij} \tag{20}$$

where w_j represents the weight value of the jth element and $\sum_{j=1}^{n} w_j = 1$.

Information entropy weighting was used to calculate the weight values w_j

$$w_j = \frac{1 - H_j}{n - \sum_{j=1}^{n} H_j} \tag{21}$$

$$H_j = -\frac{1}{\ln m}\sum_{i=1}^{m} [\mu_{ij}\ln(\mu_{ij})] \tag{22}$$

$$\mu_{ij} = \frac{r_{ij}}{\sum_{i=1}^{m} r_{ij}} \tag{23}$$

Step 3. Determining the PIS and NIS:

$$A^{+} = \{\langle\max(v_{ij}, j \in J_{-})\rangle\}, \{\langle\min(v_{ij}, j \in J_{+})\rangle\} \tag{24}$$

$$A^{-} = \{\langle\min(v_{ij}, j \in J_{-})\rangle\}, \{\langle\max(v_{ij}, j \in J_{+})\rangle\} \tag{25}$$

where J_{-} and J_{+} are associated with the negative and positive impact criteria, respectively. For the positive impact criterion, a larger value represents a better outcome. Conversely, for negative impact criteria, smaller values are better.

Step 4. Calculating the distance from PIS and NIS:

$$s_i^{+} = \sqrt{\sum_{j=1}^{n} (v_{ij} - A_j^{+})^2} \tag{26}$$

$$s_i^{-} = \sqrt{\sum_{j=1}^{n} (v_{ij} - A_j^{-})^2} \tag{27}$$

Step 5. Calculating the proximity of each scenario to the PIS to get the overall evaluation score and do normalization:

$$S_i = \frac{s_i^{-}}{s_i^{+} - s_i^{-}} \tag{28}$$

$$S^{\sim} = \frac{S_i}{\sum_{i=1}^{m} S_i} \tag{29}$$

Step 6. Leveling the set of Pareto solutions according to the value of $S^{\sim}$. The optimal compromise solution is the one with the largest $S^{\sim}$ value.

3. RESULTS AND DISCUSSION

3.1. Experimental Setup and Feature Extraction. The research in this paper is based on an NEJ-E/P200 equipment, as shown in Figure 8a. The NEJ-E/P200 was developed by our team together with Wuhan National Innovation Technology Optoelectronic Equipment Co., Ltd. The equipment consists of an environmental control system, an EHDAC system, a visual closed-loop inspection system, and a transfer curing system. The equipment has achieved closed-loop inspection.[53,54] Schematic diagram of the EHDAC system is shown in Figure 8b. There is a movement axis in the z-axis direction to adjust the coating height and is equipped with a high-precision motion stage for programed pattern coating. To facilitate the analysis of the droplet cluster deposition states, the experimental coating speed was 10 mm/s and the stainless-steel capillary tube used was 300 μm in outer diameter, 160 μm in inner diameter, and 10 mm in length. The high-voltage power supply was connected to the capillary tube, and the ink supply was available in the form of a precision flow pump and an electronic air pump. The coating substrate used was a dry, nonconductive, and nonhydrophilic glass substrate with a testing contact angle of 84.4° and a size of 100 × 100 mm, as shown in Figure 8c. Industrial cameras (Basler acA2500-14gm)

https://doi.org/10.1021/acsomega.4c05402
ACS Omega 2024, 9, 38970−38988

in X/Y directions form the real-time observation system with a lens (Moritex MML1.5-HR65D). After calibration, the state of EHDAC deposition can be detected in situ, and images can be acquired and processed. Meanwhile, a 3D optical profiler (Sensofar S-neox) was used for offline inspection, as shown in Figure 8d.

The organic ink of thin-film encapsulation (TFE) in flexible display devices was used in the research. TFE is a functional structure with a multilayer film that protects electronic devices. The ink was supplied by Wuhan China Star Optoelectronics Technology Co., Ltd. and has been orientated toward large-size industrial production line applications. The TFE ink is an acrylate-based compound that can be cured under a UV light at 365 nm. Due to confidentiality, details of the preparation and composition of the ink cannot be disclosed. Some of the physical parameters of the ink are shown in Table 1. The ink has the property of being nonvolatile, which facilitates the observation of the deposition quality of the EHDAC process.

Table 1. Physical Properties of the Organic Ink

density (ρ)	surface tension (σ)	conductivity (κ)	viscosity (μ)
985 kg/m^3	35.3 mN/m	<0.02 μS/cm	22 mPa·s

Following the design boundaries shown in Table 2, the design of experiments was run 27 times. Orthogonal coating

Table 2. Factors and Levels of the Control

operating parameter	min	center	max
voltage (v)	3000	3500	4000
pressure (kPa)	5	10	15
height (mm)	25	35	45

experiments of the TFE organic ink were completed using the EHDAC equipment. The boundaries of the parameter variables are set according to the actual coating requirements. The deposition images were processed using the EHDAC system. As shown in Figure 9, the locally deposited images were stitched together and processed. The number of pixels corresponding to the descriptive parameters of the droplet clusters was extracted, and the actual values were calculated by eq 8.

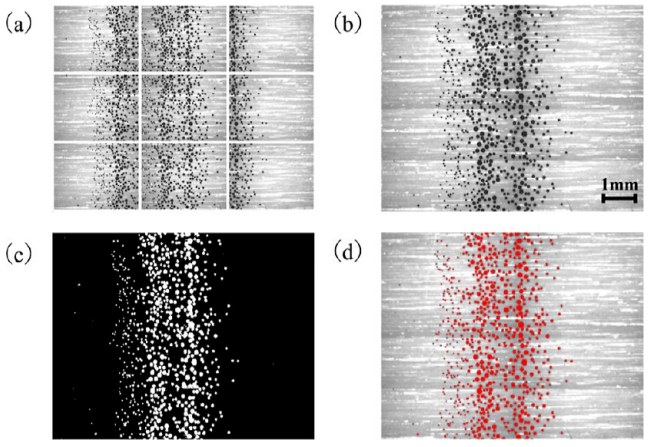

Figure 9. Local image stitching and parameter identification extraction: (a) acquisition, (b) stitching, (c) binarization, and (d) morphological filling.

3.2. Performance of the RSM Statistical Mode. For the deposition quality of EHDAC, this paper proposes to use four parameters to describe the deposition as response outputs; regression prediction models based on RSM were constructed. The values of the coefficients of the RSM model constructed according to eq 9 are shown in Table 3.

ANOVA was used to further analyze the significance of the RSM models. Table 4 gives the F-value, P-value, and Adeq-Precision (AP) values for all RSM models. From Table 4, it can be found that for the R_{ANN}, the RSM model has an F-value of 31.83 and a P-value <0.0001. Higher F-value and P-value <0.05 (i.e., confidence level of 95%) indicate that the model is significant.[55] The AP value shown is 22.65, which is much greater than 4, indicating an adequate model construction.[56] For the parameters D_{avg}, D_{CV}, and D_{MAD}, the constructed models also have a P-value <0.05. And, the F-value values were 61.64, 44.54, and 60.59 and AP values were 25.16, 24.11, and 24.51. All of the above values indicate that the RSM model is reliable. Models are sufficient to predict and describe the deposition quality of the EHDAC process. The EHDAC process can be analyzed by means of the RSM model.

3.3. Effect of Single Operating Parameters. The multiple deposition states of EHDAC are the result of the interactions and constraints between the operating parameters. The Sobol method in the global sensitivity analysis algorithm analyzes the main influencing parameters in EHDAC. The Sobol method is mainly based on the Monte Carlo variance method.[57] For the sensitivity indices of individual variables and global coupling effects, the results of the analysis are shown in Figure 10. It can be seen that R_{ANN} is strongly influenced by the coating pressure and height. And, the influence of the coating voltage is enhanced in the coupling effect. The main reason for this phenomenon is that the coating pressure mainly affects the axial velocity of the droplet group. The higher the axial velocity, the more aggregated the droplet group deposition.[58] Whereas the coating height determines the time-of-flight of the droplet clusters and droplet deflection is exacerbated by the presence of radial velocity. The coating voltage affects the initial charge of the droplet, and the Coulomb repulsion provides the acceleration in a certain direction. In addition, D_{avg} is dominated by the coating pressure, and the sensitivity indices of the coating voltage and height are low. The parameter coupling effects of models D_{CV} and D_{MAD} are not significant, and there is little difference between the independent and global sensitivity index values.

Different operating parameters determine the initial injection state. And, there is a difference in the size of the initial droplets. However, after the droplet clusters are formed, the size distribution of the droplet clusters obeys a normal distribution.[59] The forces on the droplets in the droplet clusters are different under the field coupling effect. Figure 11a–d shows the droplet cluster deposition states under four different sets of operating parameters, respectively. And, the deposition characteristics of droplet clusters are different. The red vertical line in Figure 11 represents the maximum dispersion width of the droplet clusters. It can be seen that the dispersion width of the droplet clusters is different for different operating parameters. Figure 11e plots the values of the R_{ANN} corresponding to Figure 11a–d. The R_{ANN} enables one to describe the dispersion state of the droplet clusters and to make a distinction. Furthermore, Figure 11f shows the spreading particle size distribution corresponding to Figure 11a–d. The spreading particle size distribution is different for

https://doi.org/10.1021/acsomega.4c05402
ACS Omega 2024, 9, 38970−38988

Table 3. Coefficients of the RSM Regression Model

coefficient term	R_{ANN}	D_{avg}	D_{CV}	D_{MAD}
β_0	−0.942	+94.246	+0.291	+30.484
β_1	+0.000381	−0.024	+0.000129	−0.0101
β_2	+0.0332	−0.952	−0.00843	+0.229
β_3	+0.0158	−0.292	−0.00701	−0.148
β_{11}	-8.53×10^{-6}	+0.000737	$+1.08 \times 10^{-6}$	+0.000162
β_{12}	$+2.008 \times 10^{-6}$	−0.00005	-9.38×10^{-8}	+0.000066
β_{13}	+0.000464	−0.0573	+0.000013	−0.0311
β_{22}	-5.008×10^{-8}	$+2.047 \times 10^{-6}$	-1.37×10^{-8}	$+8.33 \times 10^{-7}$
β_{23}	−0.00137	+0.141	+0.000425	+0.0613
β_{33}	−0.000353	+0.00894	+0.000028	−0.000847

Table 4. *F*-Value, *P*-Value, and AP Value Corresponding to the RSM Model

	R_{ANN}	D_{avg}	D_{CV}	D_{MAD}
F-value	31.83	61.64	44.54	60.59
P-value	<0.0001	<0.0001	<0.0001	<0.0001
AP	22.65	25.16	24.11	24.51

different deposition states. The effect of a single operating parameter on R_{ANN} is shown in Figure 12. It can be seen that when the coating voltage increases, the R_{ANN} tends to increase and then decrease. And, the R_{ANN} increases monotonically as the coating pressure decreases. As the coating height increases, R_{ANN} increases rapidly and then decreases slightly.

In addition, the local deposition images help to analyze the distribution state of the spreading droplets, as shown in Figure 13. From the distribution histogram, it can be found that the number of localized droplets increases with increasing voltage. The spreading diameter distribution of the droplets is more in line with the log-normal distribution. As the flow rate increases, the droplet spreading diameter grows larger, and the distribution interval becomes wider. As for the coating height, with the increase of coating height, the droplet spreading diameter becomes smaller. At the same time, the distribution uniformity of the spreading diameter becomes better.

3.4. Interactive Effects of Operating Parameters. Analytical models constructed through the RSM method were used to analyze the interaction surfaces between the parameters. Figure 14 illustrates the intrinsic influence between operating parameters in relation to R_{ANN} and D_{avg}. As can be seen from Figure 14a−c, at a certain coating height, the change in coating pressure has a more pronounced effect on the dispersion of droplet clusters than coating voltage. Higher voltages and lower air pressures will cause R_{ANN} to become higher and at some point reach a maximum. And, when the coating pressure is certain, the change in the coating height has a more significant effect on the value than the voltage. However, the extent of this effect is lower than that of the coating pressure. It was further verified that the effect of the flow rate on the R_{ANN} of droplet clusters was the largest.

From Figure 14d−f, it can be seen that the average spreading radius of the droplet clusters can be minimized by adjusting a higher coating voltage and a lower coating pressure at a certain height. This phenomenon is because the higher voltage creates a large electrical stress on the surface of the meniscus surface. The Taylor-cone angle of the meniscus surface will increase and the initial droplet volume will be smaller.[60] Similarly, the lower coating pressure allows for an inadequate supply of ink at the meniscus surface and a smaller initial droplet volume. Whereas under conditions of constant coating pressure, an increase in height and a increase in voltage result in a fuller atomization process and a smaller average particle size of the droplet clusters. At the same time, when the coating voltage is constant and at a low coating pressure, the effect of the height on the droplet average spreading size is not significant.

Figure 15 shows the response surface of the operating parameters to the corresponding depositional evaluation parameters D_{CV} and D_{MAD}. It can be seen that the trend of D_{CV} and D_{MAD} with voltage is the opposite. An increase in the coating voltage causes D_{CV} to increase and D_{MAD} to decrease. At the same time, as the flow increases, D_{CV} and D_{MAD}

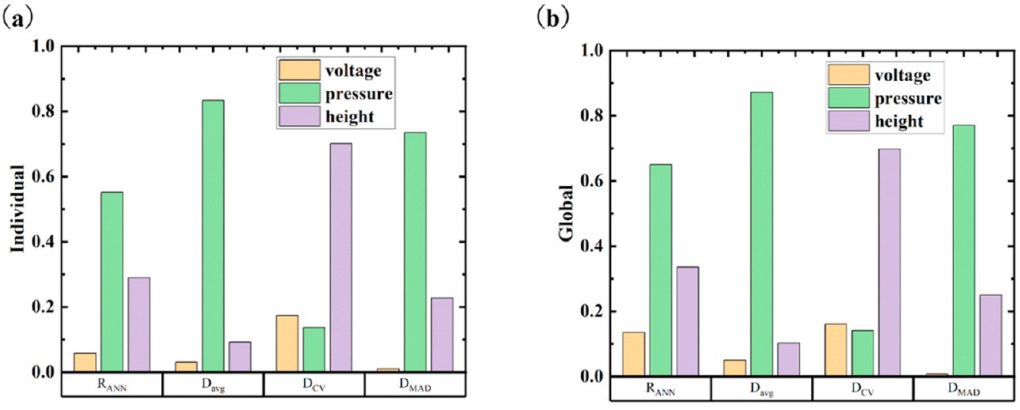

Figure 10. Results of the global sensitivity analysis. (a) Individual result and (b) global result.

https://doi.org/10.1021/acsomega.4c05402
ACS Omega 2024, 9, 38970−38988

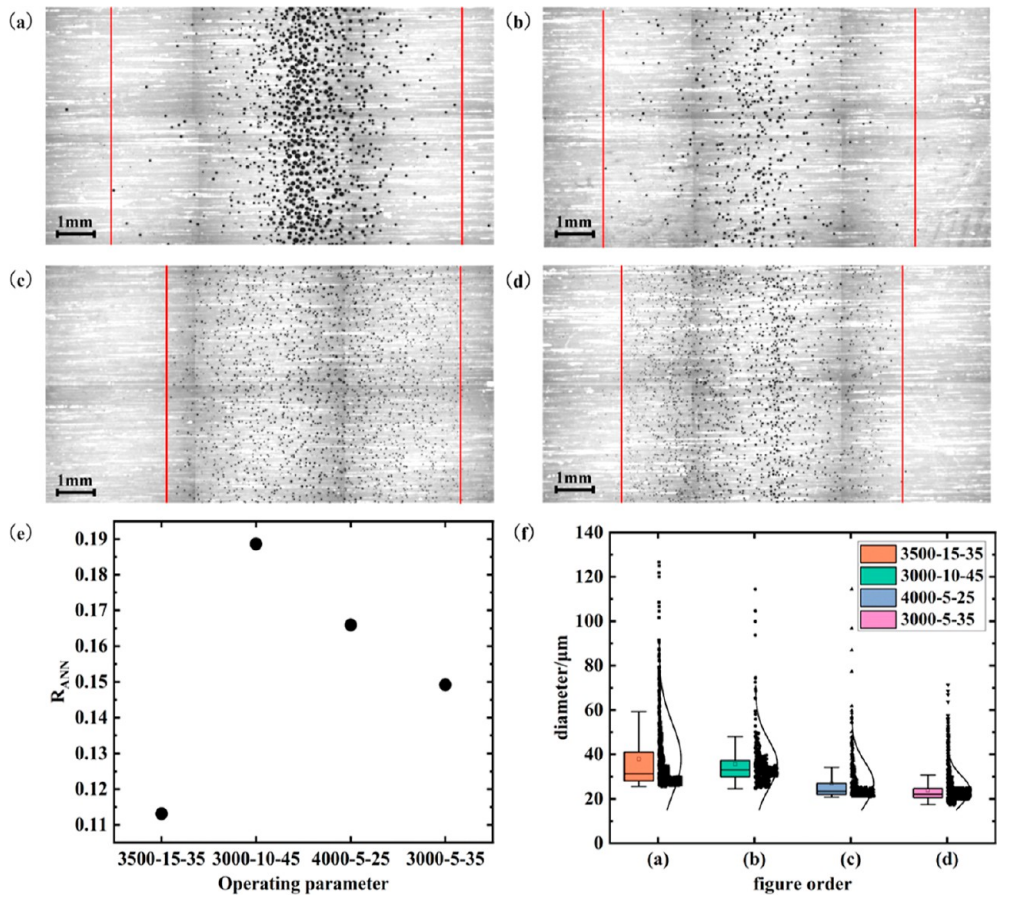

Figure 11. Degree of dispersion of the droplet clusters for different parameters. (a) 3500v 15, (b) 3000v 10, (c) 4000v 5, (d) 3000v 5 kPa 35 mm, (e) values of the R_{ANN} for the droplet clusters in (a−d), and (f) spreading particle size distribution of (a−d).

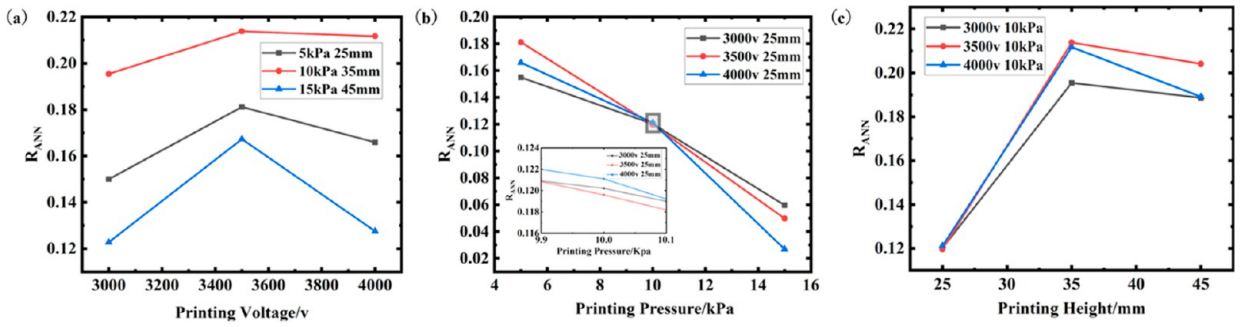

Figure 12. Effect of operating parameters on the R_{ANN}. (a) Printing voltage, (b) printing pressure, and (c) printing height.

increase. As the height increases, D_{CV} and D_{MAD} decrease. It is shown that either raising the height or lowering the pressure can help to improve the uniformity of the spreading particle size distribution.

3.5. BPNN Performance. Correlations between factors and responses were analyzed with the help of statistical methods. To further construct a more accurate data-driven model, the deposition model construction based on the BPNN network was proposed. To show the advantages of the BPNN model, the BPNN model will share the data set of the RSM model. The BPNN constructed in this paper, in which the number of hidden layers is 2 and the number of nodes is 6 and 4. And, the activation functions all use the ReLU. The regularization factor and learning rate of the BPNN are selected using cross-validation, as shown in Figure 16a. The highest prediction accuracy is achieved when the regularization parameter is 0.25 and the learning rate is 0.001. The training process using a conventional accelerator is shown in Figure 16b, where a large number of oscillations occur. At the same time, a constant learning rate from the setup is not conducive to model convergence. And, after using Nesterov's method and adding performance scheduling to control the learning rate. The training results are shown in Figure 16c. It can be seen that the loss function value is reduced to about 25 after about 20 iterations, and the model training speed is greatly increased and oscillations are reduced. In order to show the accuracy of the BPNN models, prediction validation of the model was carried out. R^2 is the ratio of predicted to total variance, representing the fit of the model construction. R^2_{adj} takes into account the effects of the independent variables and the

https://doi.org/10.1021/acsomega.4c05402
ACS Omega 2024, 9, 38970−38988

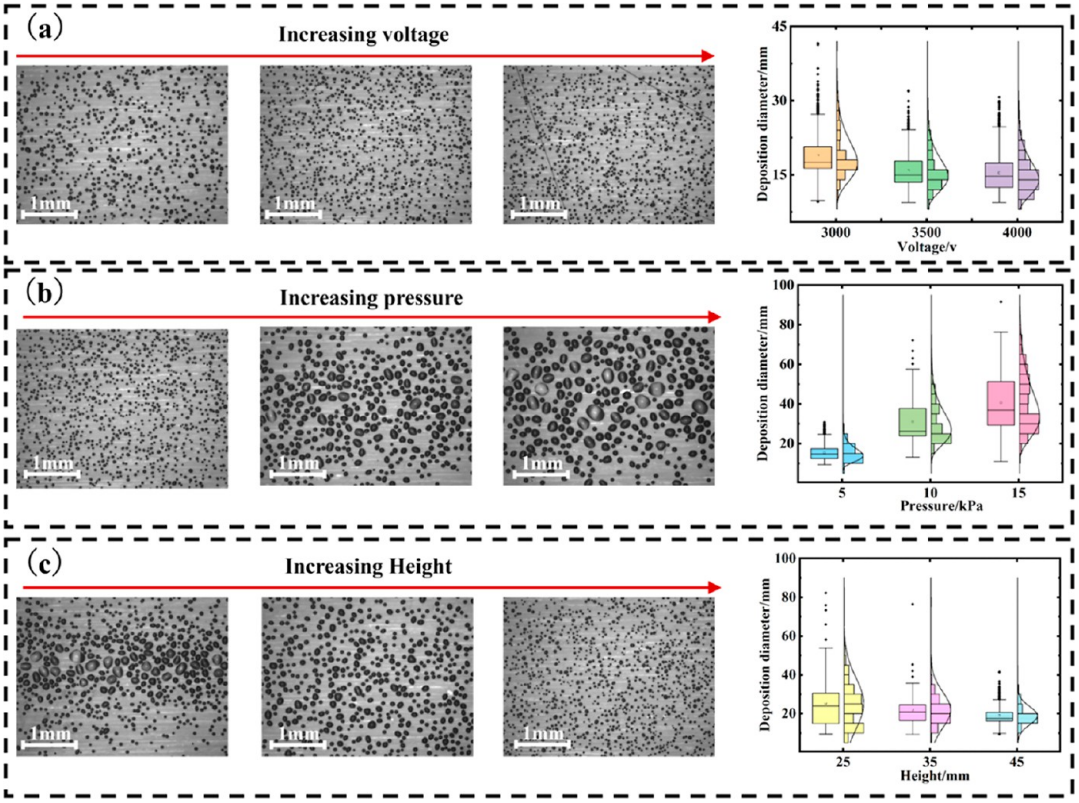

Figure 13. Local droplet cluster deposition status and distribution statistics: (a) effect of voltage increase, (b) effect of pressure increase, and (c) effect of height increase.

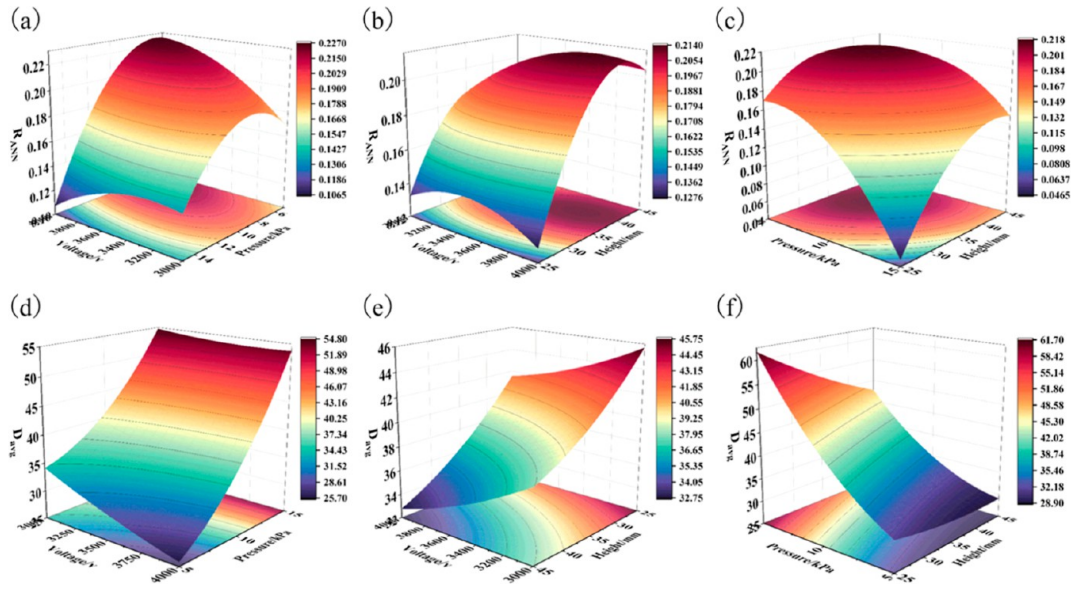

Figure 14. Relationship of the R_{ANN} and D_{avg} to the influence of operating parameters. (a) R_{ANN} with printing voltage and pressure, (b) R_{ANN} with printing voltage and height, (c) R_{ANN} with printing pressure and height, (d) D_{avg} with printing voltage and pressure, (e) D_{avg} with printing voltage and height, and (f) D_{avg} with printing pressure and height.

number of samples, avoiding the overfitting problem. From Figure 16d, the R^2 of the BPNN models are 0.944, 0.971, 0.959, and 0.969 and the R^2_{adj} are 0.914, 0.955, 0.938 and 0.954, respectively. Figure 17 shows the model prediction results of the BPNN for the depositional dispersion parameter R_{ANN} and the depositional evaluation parameters D_{avg}, D_{CV}, and D_{MAD}. The range of the error band was also plotted. It shows that the constructed model predicts the results accurately, the BPNN models are well adapted, and the accuracy is acceptable.

3.6. Multiobjective Optimization Results. In this paper, the coating performance of EHDAC is optimized by constructing deposition models with BPNN. In order to satisfy multiple objective responses simultaneously and to find the optimal deposition state in the operating parameter space, an optimization function of the form eq 17 is defined. The

https://doi.org/10.1021/acsomega.4c05402
ACS Omega 2024, 9, 38970−38988

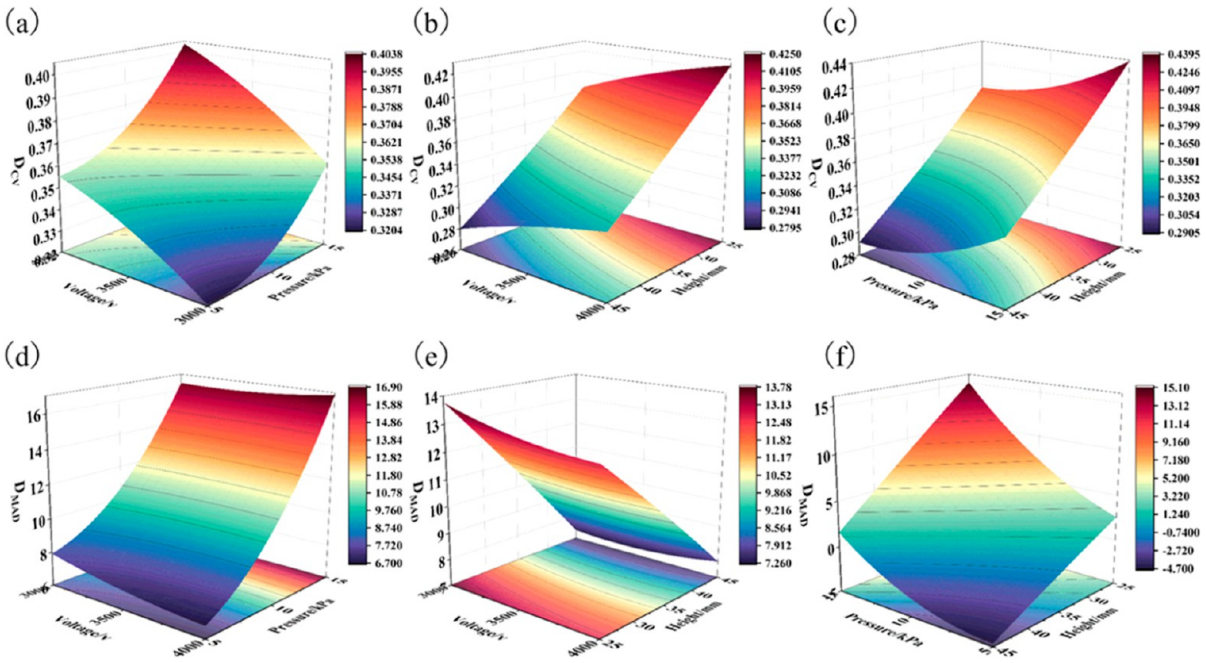

Figure 15. Relationship of the D_{CV} and D_{MAD} to the influence of operating parameters. (a) D_{CV} with printing voltage and pressure, (b) D_{CV} with printing voltage and height, (c) D_{CV} with printing pressure and height, (d) D_{MAD} with printing voltage and pressure, (e) D_{MAD} with printing voltage and height, and (f) D_{MAD} with printing pressure and height.

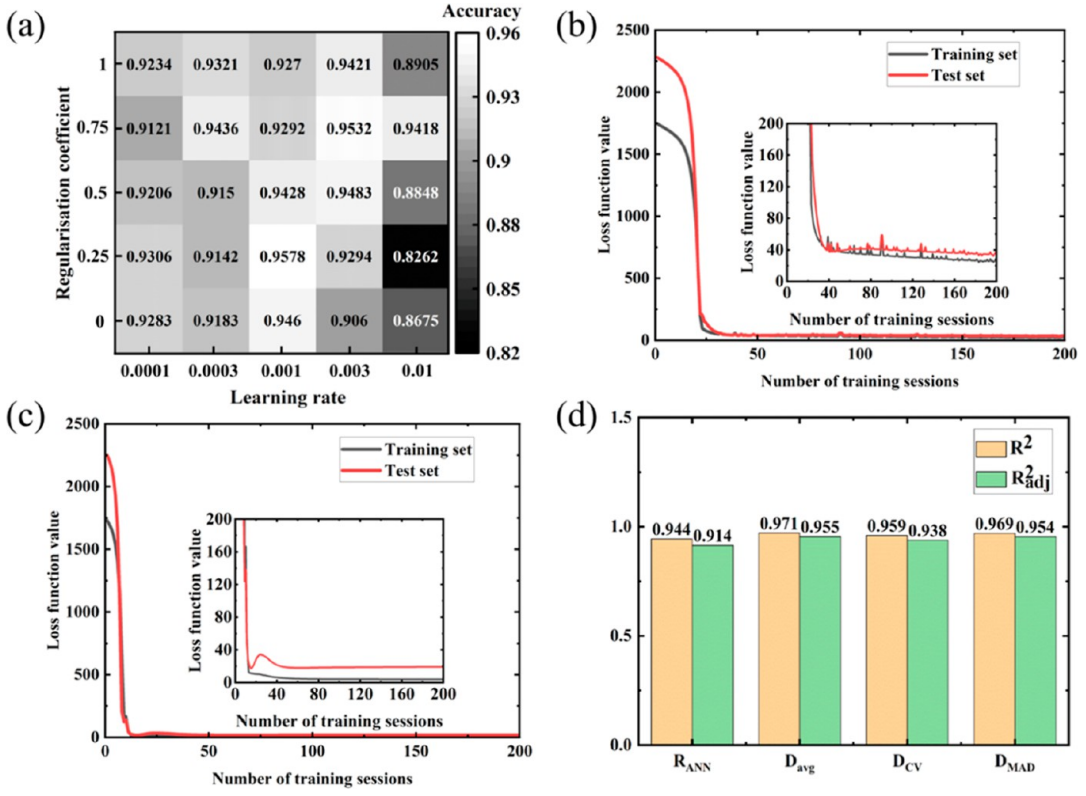

Figure 16. Performance of BPNN models. (a) Cross-validation results, (b) training process with conventional accelerator, (c) training process with Nesterov's method and performance scheduling, and (d) prediction validation.

NSGA-II algorithm is used to solve the optimization function. Pareto optimal solutions are essentially noninferior solutions to multiobjective optimization problems and can be used to solve the multiobjective optimization problem. In general, the parameters describing the deviations of the deposition distribution are considered equally important. So here, the weights of the third objective function are set as $\omega_1 = \omega_2 = 0.5$. The NSGA-II algorithm was set to have a crossover probability of 0.8, a crossover distribution index of 20, and a variance probability of 0.1. The set of Pareto front solutions for 100

https://doi.org/10.1021/acsomega.4c05402
ACS Omega 2024, 9, 38970−38988

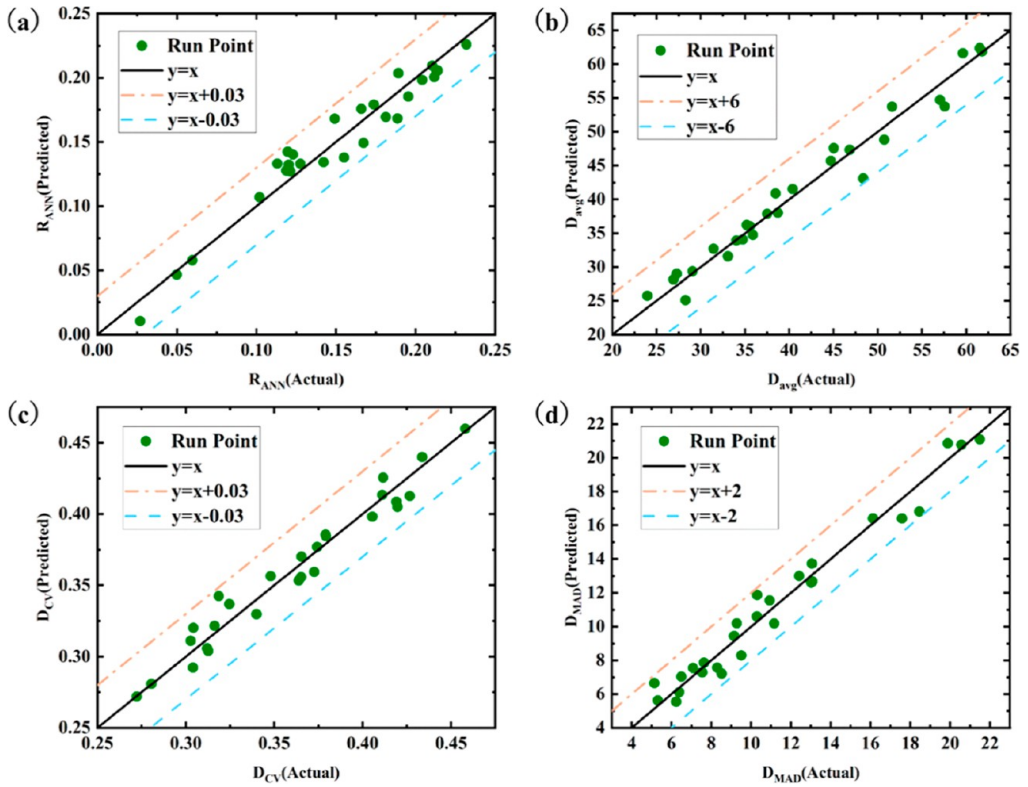

Figure 17. Results of BPNN predictions. (a) R_{ANN}, (b) D_{avg}, (c) D_{CV}, and (d) D_{MAD}.

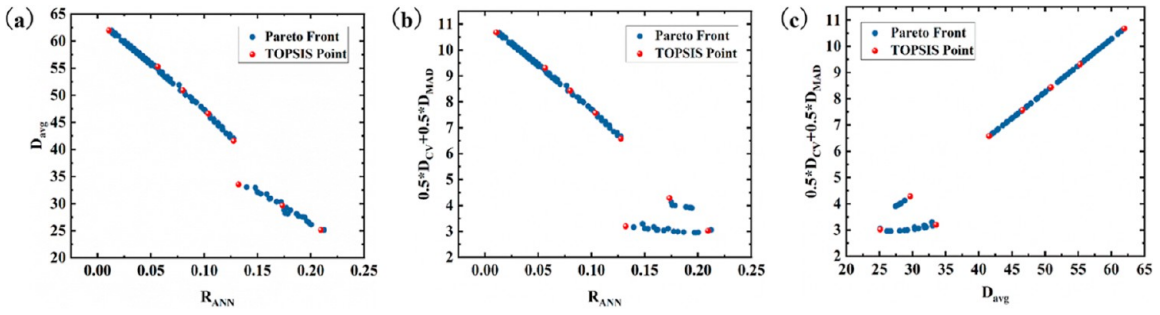

Figure 18. Pareto solution sets and recommended solutions. (a) Solution set of objective R_{ANN} and D_{avg}, (b) solution set of objective R_{ANN} and $0.5*D_{CV} + 0.5*D_{MAD}$, and (c) solution set of objective D_{avg} and $0.5*D_{CV} + 0.5*D_{MAD}$.

Table 5. Entropy Weight TOPSIS Leveling

run	v (v)	p (kPa)	h (mm)	R_{ANN}	D_{avg}	$0.5 \times D_{CV} + 0.5 \times D_{MAD}$	S_+	S_-	S_i	$S^{\sim}$
1	4000	15	24.6	0.0106	61.965	10.676	0.429	0.323	0.158	0.098
2	3880	13.6	25.3	0.0565	55.284	9.312	0.341	0.305	0.142	0.108
3	3970	12.5	25	0.0799	50.897	8.428	0.304	0.296	0.131	0.113
4	3850	11.4	25	0.1037	46.604	7.565	0.276	0.298	0.127	0.119
5	3060	10	25	0.1276	41.568	6.573	0.253	0.317	0.119	0.127
6	3840	4.8	44.7	0.1322	33.539	3.195	0.191	0.422	0.113	0.158
7	4000	5.7	25	0.1733	29.655	4.280	0.247	0.401	0.108	0.142
8	3110	3.2	44.2	0.2095	25.127	3.018	0.323	0.429	0.098	0.131

populations under 500 iterations was obtained by solving the optimization function. As shown in Figure 18, each point in the graph represents the solution obtained from the search and is labeled as level 1. It can be seen that the Pareto front exhibits competing objective functions, and there is no simultaneous minimization of more than one objective function. Of course, the range of solution sets is different for different objective function requirements. The initial population searches are continuously dispersed in the parameter space. The vast majority of nondominated solutions are derived with iterative computation. The elite population is continuously sorted and leveled and the range of the operating parameter space will also be further narrowed down. Finally, the level 1 optimized target solution set will be obtained.

Furthermore, in order to obtain the optimal compromise solution from the Pareto front solution set, 8 sets of solution

https://doi.org/10.1021/acsomega.4c05402
ACS Omega 2024, 9, 38970−38988

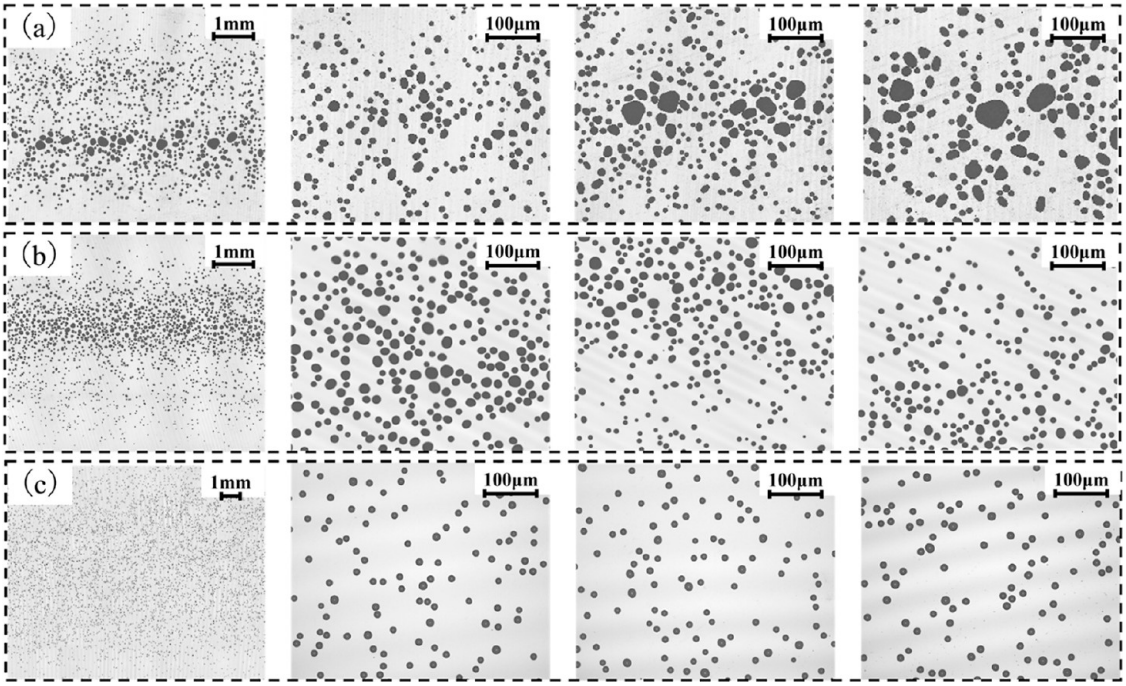

Figure 19. Deposition states corresponding to different levels of operating parameters. (a) Unoptimized droplet clusters of level 3, (b) unoptimized droplet clusters of level 2, and (c) recommended optimal process parameters.

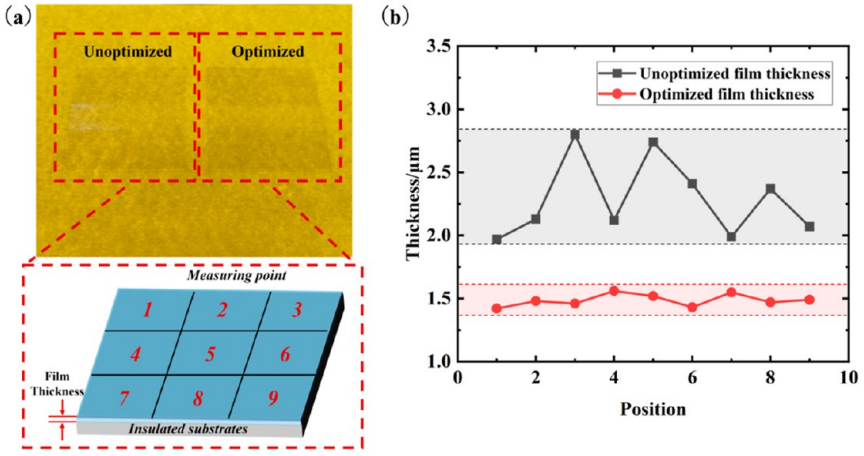

Figure 20. Validation results of thin-film manufacturing. (a) TFE fabrication and (b) results of the film thickness test.

set values in the solution set are selected for sorting and screening. Note that the screening results are only used as recommended solutions and are not necessarily optimal in the parameter space. The entropy weight TOPSIS method calculates the $S^{\sim}$ value of the solution sets and levels the 8 sets of solution sets by the magnitude of the $S^{\sim}$ value, as shown in Table 5. In Table 5, the Group 6 solutions correspond to the largest $S^{\sim}$ value. This solution is identified as the optimal compromise solution for the EHDAC process. This optimal compromise solution corresponds to the operating parameters (v = 3840v, p = 4.8 kPa, and h = 44.7 mm) that create the best deposition quality.

3.7. Validation of Optimization Results. To validate the results of the optimization strategy, the deposition quality corresponding to the optimal solution was compared to that of the unoptimized one. As shown in Figure 19, the results of the measurements were taken offline using the 3D optical profiler. Figure 19a,b shows the deposition states for the unoptimized droplet clusters of levels 3 and 2, respectively. Figure 19c shows the deposition state under the recommended optimal process parameters. It can be seen that the state of the sedimentary distribution for both levels 3 and 2 is locally skewed. Although the deposition area is small, the droplet clusters are more concentrated in the plane. However, the droplet spreading particle size and deviation are larger and the coating performance is lower. The optimal parameters result in better droplet deposition. Droplets are deposited with higher densities and smaller deviations in diffusion size and distribution. This means that at this optimal parameter, the atomization process is more adequate, and the droplets are well dispersed.

Furthermore, the film performance under optimized and unoptimized parameters is used to illustrate the effectiveness of the optimization strategy. TFE fabrication was carried out in the same manufacturing environment using an NEJ-E/P200 equipment with unoptimized and optimized operating

https://doi.org/10.1021/acsomega.4c05402
ACS Omega 2024, 9, 38970−38988

parameters, as shown in Figure 20a. Figure 20b demonstrates the results of the film thickness test, and the specific values of the film thickness are listed in Table 6. The thin-film thickness

Table 6. Overall Film Thickness

run	unoptimized film thickness (μm)	optimized film thickness (μm)
1	1.97	1.42
2	2.13	1.48
3	2.8	1.46
4	2.12	1.56
5	2.74	1.52
6	2.41	1.43
7	1.99	1.55
8	2.37	1.47
9	2.07	1.49

uniformity is calculated using eq 30. f_{max} represents the film thickness at the maximum and f_{min} represents the film thickness at the minimum.

$$f = \left(1 - \frac{f_{max} - f_{min}}{f_{max} + f_{min}}\right) \times 100\% \quad (30)$$

From the validation results, the overall thickness uniformity of the unoptimized film was calculated to be 82.6%, and the overall thickness uniformity of the unoptimized film was calculated to be 95.4%. The overall thickness quality of the film has been improved, and the uniformity has been enhanced by 12.8%. The 3D images of local film morphology acquired with the 3D optical profiler are shown in Figure 21. The films fabricated with unoptimized parameters had some mura defects. The roughnesses Ra are 49.56 and 55.71 nm, and Sa is 0.231 and 0.256 μm. The optimized film morphology, as shown in Figure 21b, has a Ra of 24.05 and 21.38 nm, Sa of 0.156 and 0.148 μm. The surface quality of the optimized film was also improved. The proposed strategy could identify the optimal operating parameters in the design space, thus systematically and efficiently optimizing the quality of the entire thin-film manufacturing process.

4. CONCLUSIONS

This paper proposes a multiobjective optimization strategy for quickly optimizing EHDAC operating parameters and enhancing efficiency and uniformity in thin-film coating on nonconductive and nonhydrophilic substrates. An in situ inspection approach is introduced in this optimization strategy to characterize the deposition quality of the charged droplet clusters by means of digital image processing methods. Four parameters, R_{ANN}, D_{avg}, D_{CV}, and D_{MAD}, are introduced to evaluate the quality of deposition. The experimental results show that these four parameters are able to accurately distinguish the quality of the deposited. The RSM model helps analyze the impact of key adjustable factors on deposition quality. The sensitivity of operating parameters to deposition state indicators was analyzed using the Sobol method. The results showed that the coating pressure had the highest degree of influence on the deposition state, followed by the coating height. The global and independent response of the coating pressure for parameters R_{ANN}, D_{avg}, and D_{MAD} exceeds 0.5%. Coating height has the highest global and independent response for D_{CV}. The results of the single effect analysis show that the dispersion of the charged droplet clusters tends to increase and then decrease when the coating voltage is increased. The dispersion decreases monotonically when the coating pressure increases, and when the coating height is decreased, the dispersion decreases rapidly and then increases slightly. At the same time, the coupling effect between operating parameters on the deposition quality is visualized by response distribution plots.

Subsequently, this paper develops a machine learning model and intelligent recommendation framework based on small data sets. The deposition quality model with high accuracy was constructed using BPNN. To find the optimal operating parameters quickly and efficiently, the multiobjective optimization strategy was used using the NSGA-II algorithm. And, the entropy weight TOPSIS method was used for screening to obtain high-quality deposited states. The combination of data-driven models and intelligent algorithms makes the manufacturing system more efficient. Under the optimal operating parameter (v = 3840v, p = 4.8 kPa, and h = 44.7 mm), the deposition of charged droplet clusters showed high quality. At the same time, film uniformity is improved by 12.8% at the optimum parameters. The surface roughness and thickness uniformity of the optimized films were better than those of the unoptimized ones. The validation results demonstrate the potential application of the multiobjective optimization strategy in micro and nano thin-film additive manufacturing on nonconductive and nonhydrophilic substrates.

Future work may focus on modeling complex intelligent models with a higher fidelity. Intelligent methods are extended with physical information to further improve the optimization

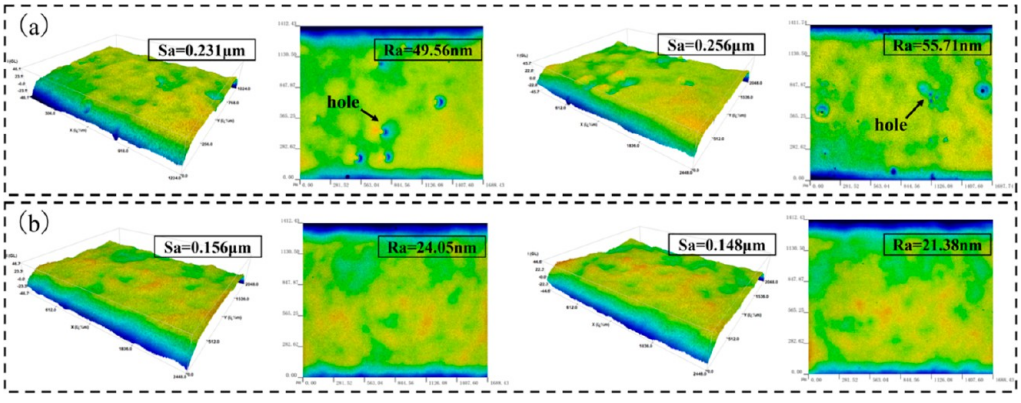

Figure 21. Validation results of local thin-film morphology. (a) Unoptimized and (b) optimized.

https://doi.org/10.1021/acsomega.4c05402
ACS Omega 2024, 9, 38970−38988

strategyand may probe more deeply into the optimization method of material properties and explore the application of intelligent learning models in organic coating.

AUTHOR INFORMATION

Corresponding Author

Jiankui Chen − *State Key Laboratory of Intelligent Manufacturing Equipment and Technology, School of Mechanical Science and Engineering, Huazhong University of Science and Technology, Wuhan 430074, PR China;* orcid.org/0000-0003-2732-2221; Email: chenjk@hust.edu.cn

Authors

Chao Hu − *State Key Laboratory of Intelligent Manufacturing Equipment and Technology, School of Mechanical Science and Engineering, Huazhong University of Science and Technology, Wuhan 430074, PR China;* orcid.org/0009-0006-0507-7391

Wei Chen − *State Key Laboratory of Intelligent Manufacturing Equipment and Technology, School of Mechanical Science and Engineering, Huazhong University of Science and Technology, Wuhan 430074, PR China;* orcid.org/0000-0003-3983-0063

Wei Tang − *Wuhan National Innovation Technology Optoelectronics Equipment Co., Ltd, Wuhan 430074, PR China*

Guozhen Wang − *State Key Laboratory of Intelligent Manufacturing Equipment and Technology, School of Mechanical Science and Engineering, Huazhong University of Science and Technology, Wuhan 430074, PR China*

Fei Pan − *State Key Laboratory of Intelligent Manufacturing Equipment and Technology, School of Mechanical Science and Engineering, Huazhong University of Science and Technology, Wuhan 430074, PR China*

Zhouping Yin − *State Key Laboratory of Intelligent Manufacturing Equipment and Technology, School of Mechanical Science and Engineering, Huazhong University of Science and Technology, Wuhan 430074, PR China*

Complete contact information is available at: https://pubs.acs.org/10.1021/acsomega.4c05402

Author Contributions

Chao Hu: data curation, writing−original draft, conceptualization, methodology, and validation. **Jiankui Chen:** writing−review and editing, supervision, and funding acquisition. **Wei Chen:** writing−review and editing and formal analysis. **Wei Tang:** software. **Guozhen Wang:** methodology and formal analysis. **Fei Pan:** methodology and validation. **Zhouping Yin:** writing−review and editing, resources, and funding acquisition.

Notes

The authors declare no competing financial interest.

ACKNOWLEDGMENTS

This research was financially supported by the CUI CAN Program of Guangdong Province (CC/XM-202402ZJ0102), the National Key Research and Development Program of China (2018YFA0703203), and the National Natural Science Foundation of China (51975236).

REFERENCES

(1) Chowdhury, M. R.; Steffes, J.; Huey, B. D.; McCutcheon, J. R. 3D printed polyamide membranes for desalination. *Sci.* **2018**, *361*, 682−686.

(2) Xin, G.; Sun, H.; Hu, T.; Fard, H. R.; Sun, X.; Koratkar, N.; Borca-Tasciuc, T.; Lian, J. Large-Area Freestanding Graphene Paper for Superior Thermal Management. *Adv. Mater.* **2014**, *26*, 4521−4526.

(3) Gañán-Calvo, A. M.; López-Herrera, J. M.; Herrada, M. A.; Ramos, A.; Montanero, J. M. Review on the physics of electrospray: From electrokinetics to the operating conditions of single and coaxial Taylor cone-jets, and AC electrospray. *J. Aerosol Sci.* **2018**, *125*, 32−56.

(4) Conde, J. J.; Ferreira-Aparicio, P.; Chaparro, A. M. Electrospray Deposition: A Breakthrough Technique for Proton Exchange Membrane Fuel Cell Catalyst Layer Fabrication. *ACS Appl. Energy Mater.* **2021**, *4*, 7394−7404.

(5) Rosell-Llompart, J.; Grifoll, J.; Loscertales, I. G. Electrosprays in the cone-jet mode: From Taylor cone formation to spray development. *J. Aerosol Sci.* **2018**, *125*, 2−31.

(6) Jaworek, A.; Sobczyk, A. T. Electrospraying route to nanotechnology: An overview. *J. Electrost.* **2008**, *66*, 197−219.

(7) Chen, N.; He, C.; Pang, S. Additive manufacturing of energetic materials: Tailoring energetic performance via printing. *J. Mater. Sci. Nanotechnol.* **2022**, *127*, 29−47.

(8) Gao, D.; G Zhou, J. Designs and applications of electrohydrodynamic 3D printing. *Int. J. Bioprint.* **2018**, *5*, 172.

(9) Yan, J.-X.; Leng, Y.-C.; Guo, Y.-N.; Wang, G.-Q.; Gong, H.; Guo, P.-Z.; Tan, P.-H.; Long, Y.-Z.; Liu, X.-L.; Han, W.-P. Highly Conductive Graphene Paper with Vertically Aligned Reduced Graphene Oxide Sheets Fabricated by Improved Electrospray Deposition Technique. *ACS Appl. Mater. Interfaces* **2019**, *11*, 10810−10817.

(10) Kim, S.-Y.; Kim, K.; Hwang, Y. H.; Park, J.; Jang, J.; Nam, Y.; Kang, Y.; Kim, M.; Park, H. J.; Lee, Z.; Choi, J.; Kim, Y.; Jeong, S.; Bae, B.-S.; Park, J.-U. High-resolution electrohydrodynamic inkjet printing of stretchable metal oxide semiconductor transistors with high performance. *Nanoscale* **2016**, *8*, 17113−17121.

(11) Ding, Y.; Zhu, C.; Liu, J.; Duan, Y.; Yi, Z.; Xiao, J.; Wang, S.; Huang, Y.; Yin, Z. Flexible small-channel thin-film transistors by electrohydrodynamic lithography. *Nanoscale* **2017**, *9*, 19050−19057.

(12) Zong, H.; Xia, X.; Liang, Y.; Dai, S.; Alsaedi, A.; Hayat, T.; Kong, F.; Pan, J. H. Designing function-oriented artificial nanomaterials and membranes via electrospinning and electrospraying techniques. *Mater. Sci. Eng., C* **2018**, *92*, 1075−1091.

(13) Yang, L.; Liu, Y.; Sun, L.; Zhao, C.; Chen, G.; Zhao, Y. Biomass Microcapsules with Stem Cell Encapsulation for Bone Repair. *Nano-Micro Lett.* **2022**, *14*, 4.

(14) Luo, Y.; Li, Y.; Feng, X.; Pei, Y.; Zhang, Z.; Wang, L.; Zhao, Y.; Lu, B.; Zhu, B. Triboelectric nanogenerators with porous and hierarchically structured silk fibroin films via water electrospray-etching technology. *Nano Energy* **2020**, *75*, 104974.

(15) Zhu, C.; Fu, Y.; Yu, Y. Designed Nanoarchitectures by Electrostatic Spray Deposition for Energy Storage. *Adv. Mater.* **2019**, *31*, 1803408.

(16) Yu, M.; Ahn, K. H.; Lee, S. J. Design optimization of ink in electrohydrodynamic jet printing: Effect of viscoelasticity on the formation of Taylor cone jet. *Mater. Des.* **2016**, *89*, 109−115.

(17) Lee, A.; Jin, H.; Dang, H.-W.; Choi, K.-H.; Ahn, K. H. Optimization of Experimental Parameters To Determine the Jetting Regimes in Electrohydrodynamic Printing. *Langmuir* **2013**, *29*, 13630−13639.

(18) Hartman, R. P. A.; Brunner, D. J.; Camelot, D. M. A.; Marijnissen, J. C. M.; Scarlett, B. Jet Break-Up in Electrohydrodynamic Atomization in the Cone-Jet Mode. *J. Aerosol Sci.* **2000**, *31*, 65−95.

(19) Hartman, R. P. A.; Brunner, D. J.; Camelot, D. M. A.; Marijnissen, J. C. M.; Scarlett, B. Electrohydrodynamic Atomization

https://doi.org/10.1021/acsomega.4c05402
ACS Omega 2024, 9, 38970−38988

in the Cone−Jet Mode Physical Modeling of the Liquid Cone and Jet. *J. Aerosol Sci.* **1999**, *30*, 823−849.
(20) Hayati, I.; Bailey, A. I.; Tadros, Th.F. Investigations into the mechanisms of electrohydrodynamic spraying of liquids: I. Effect of electric field and the environment on pendant drops and factors affecting the formation of stable jets and atomization. *J. Colloid Interface Sci.* **1987**, *117*, 205−221.
(21) Huo, Y.; Wang, J.; Zuo, Z.; Fan, Y. Visualization of the evolution of charged droplet formation and jet transition in electrostatic atomization. *Phys. Fluids* **2015**, *27*, 114105.
(22) Yang, S.; Wang, Z.; Kong, Q.; Li, B.; Wang, J. Visualization on electrified micro-jet instability from Taylor cone in electrohydrodynamic atomization. *Chin. J. Chem. Eng.* **2022**, *44*, 456−465.
(23) Wang, Q.; Wang, Z.; Yang, S.; Li, B.; Xu, H.; Yu, K.; Wang, J. Experimental study on electrohydrodynamic atomization (EHDA) in stable cone-jet with middle viscous and low conductive liquid. *Exp. Therm. Fluid Sci.* **2021**, *121*, 110260.
(24) Jaworek, A. Electrospray droplet sources for thin film deposition. *J. Mater. Sci.* **2007**, *42*, 266−297.
(25) Tang, K.; Gomez, A. On the structure of an electrostatic spray of monodisperse droplets. *Phys. Fluids* **1994**, *6*, 2317−2332.
(26) Leeuwenburgh, S. C. G.; Heine, M. C.; Wolke, J. G. C.; Pratsinis, S. E.; Schoonman, J.; Jansen, J. A. Morphology of calcium phosphate coatings for biomedical applications deposited using Electrostatic Spray Deposition. *Thin Solid Films* **2006**, *503*, 69−78.
(27) Kingsley, B. J.; Chiarot, P. R. Polyimide Films Manufactured Using Partially Wet Electrospray Deposition. *ACS Appl. Polym. Mater.* **2023**, *5*, 1797−1809.
(28) Wang, R.; Deng, J.; Zhang, Z.; Lu, Y.; Li, X.; Ge, D. Preparation and infrared properties of Ni3Al−Cr3C2 composite films deposited by electrohydrodynamic atomization technology. *Mater. Chem. Phys.* **2022**, *278*, 125654.
(29) Rietveld, I. B.; Kobayashi, K.; Yamada, H.; Matsushige, K. Electrospray Deposition, Model, and Experiment: Toward General Control of Film Morphology. *J. Phys. Chem. B* **2006**, *110*, 23351−23364.
(30) Rietveld, I. B.; Kobayashi, K.; Yamada, H.; Matsushige, K. Process parameters for fast production of ultra-thin polymer film with electrospray deposition under ambient conditions. *J. Colloid Interface Sci.* **2009**, *339*, 481−488.
(31) Sındıraç, C.; Akkurt, S. Microstructural investigation of the effect of electrospraying parameters on LSCF films. *Int. J. Hydrogen Energy* **2020**, *45*, 35139−35148.
(32) Huang, S.; Mansouri, J.; Le-Clech, P.; Leslie, G.; Tang, C. Y.; Fane, A. G. A comprehensive review of electrospray technique for membrane development: Current status, challenges, and opportunities. *J. Membr. Sci.* **2022**, *646*, 120248.
(33) Zhang, H.; Choi, J. P.; Moon, S. K.; Ngo, T. H. A hybrid multi-objective optimization of aerosol jet printing process via response surface methodology. *Addit. Manuf.* **2020**, *33*, 101096.
(34) Singh, G.; Missiaen, J.-M.; Bouvard, D.; Chaix, J.-M. Copper extrusion 3D printing using metal injection moulding feedstock: Analysis of process parameters for green density and surface roughness optimization. *Addit. Manuf.* **2021**, *38*, 101778.
(35) Suzuki, A.; Shiba, Y.; Ibe, H.; Takata, N.; Kobashi, M. Machine-learning assisted optimization of process parameters for controlling the microstructure in a laser powder bed fused WC/Co cemented carbide. *Addit. Manuf.* **2022**, *59*, 103089.
(36) Liu, Y.; Yin, S.; Liu, Z.; Zhang, H. A machine learning framework for process optimization in aerosol jet 3D printing. *Flexible Printed Electron.* **2023**, *8*, 025017.
(37) Kong, Q.; Yang, S.; Wang, Q.; Wang, Z.; Dong, Q.; Wang, J. Dynamics of electrified jets in electrohydrodynamic atomization. *Case Stud. Therm. Eng.* **2022**, *29*, 101725.
(38) Son, S.; Lee, S.; Choi, J. Fine metal line patterning on hydrophilic non-conductive substrates based on electrohydrodynamic printing and laser sintering. *J. Electrost.* **2014**, *72*, 70−75.
(39) Zhang, X.; Lies, B.; Lyu, H.; Qin, H. In-situ monitoring of electrohydrodynamic inkjet printing via scalar diffraction for printed droplets. *J. Manuf. Syst.* **2019**, *53*, 1−10.
(40) Gong, T.; Li, L.; Shi, M.; Kang, L.; Gao, L.; Li, J. Performance assessment and optimization of a thin-film thermoelectric cooler for on-chip transient thermal management. *Appl. Therm. Eng.* **2023**, *224*, 120079.
(41) Pulipaka, A.; Gide, K. M.; Beheshti, A.; Bagheri, Z. S. Effect of 3D printing process parameters on surface and mechanical properties of FFF-printed PEEK. *J. Manuf. Process.* **2023**, *85*, 368−386.
(42) Paturi, U. M. R.; Reddy, N. S.; Cheruku, S.; Narala, S. K. R.; Cho, K. K.; Reddy, M. M. Estimation of coating thickness in electrostatic spray deposition by machine learning and response surface methodology. *Surf. Coat. Technol.* **2021**, *422*, 127559.
(43) Bhosekar, A.; Ierapetritou, M. Advances in surrogate based modeling, feasibility analysis, and optimization: A review. *Comput. Chem. Eng.* **2018**, *108*, 250−267.
(44) Brunton, S. L.; Noack, B. R.; Koumoutsakos, P. Machine Learning for Fluid Mechanics. *Annu. Rev. Fluid. Mech.* **2020**, *52*, 477−508.
(45) Wang, J.; Li, Y.; Gao, R. X.; Zhang, F. Hybrid physics-based and data-driven models for smart manufacturing: Modelling, simulation, and explainability. *J. Manuf. Syst.* **2022**, *63*, 381−391.
(46) Yao, D.; Wang, J.; Luo, H.; Wu, Y.; An, X. Thermal behavior and control during multi-track laser powder bed fusion of 316 L stainless steel. *Addit. Manuf.* **2023**, *70*, 103562.
(47) Walkington, N. J. Nesterov's Method for Convex Optimization. *SIAM Rev.* **2023**, *65*, 539−562.
(48) Xiao, Y.; Jiang, Z.; Gu, Q.; Yan, W.; Wang, R. A novel approach to CNC machining center processing parameters optimization considering energy-saving and low-cost. *J. Manuf. Syst.* **2021**, *59*, 535−548.
(49) Zhu, Q.; Huang, S.; Wang, G.; Moghaddam, S. K.; Lu, Y.; Yan, Y. Dynamic reconfiguration optimization of intelligent manufacturing system with human-robot collaboration based on digital twin. *J. Manuf. Syst.* **2022**, *65*, 330−338.
(50) Gu, P.; Zhu, C.; Mura, A.; Maculotti, G.; Goti, E. Grinding performance and theoretical analysis for a high volume fraction SiCp/Al composite. *J. Manuf. Process.* **2022**, *76*, 796−811.
(51) Hadibafekr, S.; Mirzaee, I.; Khalilian, M.; Shirvani, H. Thermo-entropic analysis and multi-objective optimization of wavy lobed heat exchanger tube using DOE, RSM, and NSGA II algorithm. *Int. J. Therm. Sci.* **2023**, *184*, 107921.
(52) Singh, P.; Meena, N. K.; Yang, J.; Vega-Fuentes, E.; Bishnoi, S. K. Multi-criteria decision making monarch butterfly optimization for optimal distributed energy resources mix in distribution networks. *Appl. Energy* **2020**, *278*, 115723.
(53) Zhang, Z.; Chen, J.; Yang, H.; Yin, Z. Accurate Measurements of Droplet Volume With Coherence Scanning Interferometry. *IEEE Trans. Instrum. Meas.* **2023**, *72*, 1−15.
(54) Yue, X.; Chen, J.; Li, Y.; Li, X.; Zhu, H.; Yin, Z. Intelligent control system for droplet volume in inkjet printing based on stochastic state transition soft actor−critic DRL algorithm. *J. Manuf. Syst.* **2023**, *68*, 455−464.
(55) Zaferani, S. P. G.; Emami, M. R. S.; Amiri, M. K.; Binaeian, E. Optimization of the removal Pb (II) and its Gibbs free energy by thiosemicarbazide modified chitosan using RSM and ANN modeling. *Int. J. Biol. Macromol.* **2019**, *139*, 307−319.
(56) Song, H.; Dan, J.; Li, J.; Du, J.; Xiao, J.; Xu, J. Experimental study on the cutting force during laser-assisted machining of fused silica based on the Taguchi method and response surface methodology. *J. Manuf. Process.* **2019**, *38*, 9−20.
(57) Lei, T.; Liu, H.; Ma, C.; Han, J. Optimal Design of Droplet Ejection for PZT Printhead Based on Surrogate Model. *Appl. Sci.* **2022**, *12*, 11683.
(58) Hartman, R. P. A.; Borra, J.-P.; Brunner, D. J.; Marijnissen, J. C. M.; Scarlett, B. The evolution of electrohydrodynamic sprays produced in the cone-jet mode, a physical model. *J. Electrost.* **1999**, *47*, 143−170.

https://doi.org/10.1021/acsomega.4c05402
ACS Omega 2024, 9, 38970−38988

(59) Juan, L. de.; Mora, J. F. de la. Charge and Size Distributions of Electrospray Drops. *J. Colloid Interface Sci.* **1997**, *186*, 280−293.
(60) Ryan, C. N.; Smith, K. L.; Stark, J. P. W. The influence of geometry on the flow rate sensitivity to applied voltage within cone-jet mode electrospray. *J. Appl. Phys.* **2012**, *112*, 114510.

https://doi.org/10.1021/acsomega.4c05402
ACS Omega 2024, 9, 38970−38988